

Calibration of the JUICE RWI Antennas by Numerical Simulation

G. Fischer, M. Panchenko, W. Macher, Y. Kasaba, H. Misawa, M. Tokarz, L. Wisniewski, B. Cecconi, J. Bergman, J. -E. Wahlund

▶ **To cite this version:**

G. Fischer, M. Panchenko, W. Macher, Y. Kasaba, H. Misawa, et al.. Calibration of the JUICE RWI Antennas by Numerical Simulation. Radio Science, 2021, 56, 10.1029/2021RS007309 . insu-03713745

HAL Id: insu-03713745

https://insu.hal.science/insu-03713745

Submitted on 6 Aug 2022

HAL is a multi-disciplinary open access archive for the deposit and dissemination of scientific research documents, whether they are published or not. The documents may come from teaching and research institutions in France or abroad, or from public or private research centers.

L'archive ouverte pluridisciplinaire **HAL**, est destinée au dépôt et à la diffusion de documents scientifiques de niveau recherche, publiés ou non, émanant des établissements d'enseignement et de recherche français ou étrangers, des laboratoires publics ou privés.

Copyright

Check for updates

Radio Science

RESEARCH ARTICLE
10.1029/2021RS007309

Calibration of the JUICE RWI Antennas by Numerical Simulation

G. Fischer[1], M. Panchenko[1], W. Macher[1], Y. Kasaba[2], H. Misawa[2], M. Tokarz[3], L. Wisniewski[3], B. Cecconi[4], J. Bergman[5], and J.-E. Wahlund[5]

[1]Space Research Institute, Austrian Academy of Sciences, Graz, Austria, [2]Planetary Plasma and Atmospheric Research Center, Tohoku University, Sendai, Japan, [3]Astronika, Warsaw, Poland, [4]LESIA, Observatoire de Paris, PSL, CNRS, Meudon, France, [5]Swedish Institute of Space Physics, Uppsala, Sweden

M. Panchenko left from Space Research Institute of the Austrian Academy of Sciences.

Key Points:

- The antennas of the Radio Wave Instrument (RWI) onboard Jupiter Icy Moons Explorer were calibrated by numerical computer simulations
- Results include the calculation of effective lengths vectors, antenna impedances, and high-frequency characteristics
- Strong active radar pulses should not harm the RWI and Langmuir probe receivers

Correspondence to:

G. Fischer,
georg.fischer@oeaw.ac.at

Citation:

Fischer, G., Panchenko, M., Macher, W., Kasaba, Y., Misawa, H., Tokarz, M., et al. (2021). Calibration of the JUICE RWI antennas by numerical simulation. *Radio Science*, *56*, e2021RS007309. https://doi.org/10.1029/2021RS007309

Received 5 MAY 2021
Accepted 11 OCT 2021

Author Contributions:

Conceptualization: G. Fischer
Formal analysis: W. Macher
Funding acquisition: G. Fischer
Investigation: G. Fischer, M. Panchenko
Methodology: G. Fischer, M. Panchenko, W. Macher, Y. Kasaba, H. Misawa
Project Administration: G. Fischer, Y. Kasaba, L. Wisniewski, J. Bergman, J.-E. Wahlund
Software: G. Fischer, M. Panchenko
Supervision: G. Fischer
Validation: G. Fischer, M. Panchenko, W. Macher, B. Cecconi
Visualization: G. Fischer, Y. Kasaba, M. Tokarz, L. Wisniewski
Writing – original draft: G. Fischer
Writing – review & editing: G. Fischer, M. Panchenko, W. Macher, Y. Kasaba, H. Misawa, M. Tokarz, L. Wisniewski, B. Cecconi, J. Bergman, J.-E. Wahlund

© 2021. American Geophysical Union. All Rights Reserved.

Abstract The reception properties of the Radio Wave Instrument (RWI) onboard JUICE (Jupiter Icy Moons Explorer) have been determined using numerical methods applied to a mesh-grid model of the spacecraft. The RWI is part of the RPWI (Radio and Plasma Wave Investigation) and consists of three perpendicular dipoles mounted on a long boom. We determined their effective lengths vectors and capacitive impedances of 8–9 pF. We also investigated the change in effective antenna angles as a function of solar panel rotation and calculated the directivity of the antennas at higher frequencies up to the maximum frequency of 45 MHz of the receiver. We found that the RWI dipoles can be used for direction-finding with an accuracy of 2° up to a frequency of 1.5 MHz. Additionally we calculated the influence of strong pulses from the JUICE active radar on RPWI and found that they should do no harm to its sensors and receivers.

Plain Language Summary In this paper we calculate the reception properties of the antennas of the Radio Wave Instrument (RWI) onboard the JUICE (Jupiter Icy Moons Explorer) spacecraft using numerical computer simulations. The RWI is part of the RPWI (Radio and Plasma Wave Investigation) and consists of three perpendicular dipoles mounted on a long boom. With this antenna system the scientists want to determine the intensity, the polarization, and the incoming radio wave direction of Jovian radio emissions. This can only be properly done when the reception properties of the antennas are well known, and for this necessary calibration we calculate the so-called effective length vector. It can describe the reception properties of an antenna, being constant (direction-independent) when the wavelength is large compared to the dimensions of the spacecraft. The antenna pattern of an RWI dipole has a toroidal shape like a donut at lower frequencies, but gets multiple lobes at higher frequencies. We also calculated the influence of the strong pulses from the JUICE active radar on the RPWI sensors and receivers and found that no harm should be done to them.

1. Introduction

JUICE (Jupiter Icy Moons Explorer) is an ESA L-class mission (European Space Agency Large mission) that is planned to be launched in August or September 2022. After a cruise of almost nine years with four Earth flybys and one Venus flyby it should go into a Jovian orbit in summer 2031. During its tour around Jupiter the spacecraft will stay in the equatorial plane for most of the time except for the so-called Jupiter high latitude phase lasting for about one year. There will be several flybys of the icy moons Europa, Callisto, and Ganymede, and finally JUICE should go into a Ganymede orbit. The end of the nominal mission is planned for autumn 2035. The overarching goal of the JUICE mission is to study the emergence of habitable worlds around gas giants and to study the Jupiter system as an archetype for gas giants (Grasset et al., 2013). JUICE is a solar powered spacecraft, and its large solar array should deliver a power of about 760 Watts. The dry mass of the spacecraft will be around 2.2 tons, and with 2.9 tons of propellant the total mass will be larger than 5 tons. Its 2.4 m diameter high gain antenna will enable a data transmission rate of about 2.3 Gb/day.

The JUICE payload consists of 10 scientific instruments plus one experiment that uses the spacecraft communication system with ground-based instruments. Four instruments belong to the remote sensing package, three to the geophysical package, and three to the so-called in-situ package. The Radio and Plasma Wave Investigation (RPWI) instrument formally belongs to the latter category. However, it is a versatile

instrument that can make both remote-sensing and in-situ measurements of radio and plasma waves, respectively. It has three different kind of sensors, which are the three linear antennas of the Radio Wave Instrument (RWI), four Langmuir Probes, and a Search Coil Magnetometer (SCM). In summer 2019 RPWI was delivered to Airbus for integration on the spacecraft. It was mainly manufactured in Sweden with multiple hardware contributions from other countries like France, Poland, Czech Republic, and Japan. RPWI will cover the full frequency range of the Jovian radio spectrum from DC to 45 MHz comprising the QP (quasi-periodic) bursts, kilometric emissions (KOM), hectometric emission (HOM) and decametric radio emissions (DAM). Its goniopolarimetric capabilities will allow measuring the radio wave polarization, locating the radio sources and measuring their sizes, monitoring the magnetospheric activity, and inferring the plasma characteristics along the wave propagation path. Previous radio and plasma wave instruments of spacecraft at Jupiter did not have such capabilities (Voyagers, Galileo, Juno) or they performed only short flybys (Voyagers, Ulysses, Cassini). RPWI will encounter many different space plasma environments around Jupiter's icy moons and in Jupiter's magnetosphere. The environment of Ganymede is of particular interest for magnetospheric science, since Ganymede has an own intrinsic magnetic field and represents a mini-magnetosphere within Jupiter's large magnetosphere, where radio and plasma waves can also be detected. For this purpose, RPWI will use several different sensors and receivers.

There are four Langmuir probes (LP) located at the tips of four ~3 m long booms which will perform plasma and three-dimensional electric field measurements. The LPs are connected to a 14-bit LP and MIME (Mutual IMpedance Experiment) transceiver for the reception and transmission of waves up to 1.5 MHz, and the whole subsystem is called Langmuir Probe Plasma Wave Instrument (LP-PWI). There is a SCM for magnetic field measurements from DC up to 20 kHz. There are the three dipole antennas of the RWI, which are connected to a 14-bit High Frequency receiver ranging from 80 kHz to 45 MHz. Both SCM and RWI antennas are mounted on the 10.6 m long magnetometer (MAG) boom. The RWI antenna triad is located ~8.5 m away from the foot point of the MAG boom on the spacecraft body. The RWI antennas are connected to pre-amplifiers, which are located very close to the foot points of the antennas. This is to avoid large base capacitances caused by long coax cables, since the main electronic box with the High Frequency receiver is located inside the spacecraft. The three antennas enable the determination of the electric field vector, Poynting flux, the wave polarization (Stokes parameters), and the incoming radio wave direction (Carozzi et al., 2000; Cecconi & Zarka, 2005; Ladreiter et al., 1995). Our calibration effort in this paper focuses on the three linear RWI dipoles of 2.5 m tip-to-tip length each.

The highly conducting spacecraft body is electromagnetically coupled to the antennas, and the antenna receiving properties strongly depend on the spacecraft shape. It is impossible to find an analytical solution of the surface current distribution in closed form, owing to the complex structure of the antennas-spacecraft system. Therefore, computer simulations and experimental methods are used to find the reception properties of the antennas. One of the experimental methods is called rheometry. It is based on an electrolytic tank measurement in which an electric field is applied to a scaled model immersed in water. Rheometry has been made for the radio antenna calibration of several spacecraft in the last 25 years, for example, Cassini (Rucker et al., 1996), STEREO (Macher et al., 2007), Resonance (Sampl et al., 2012), or Juno (Sampl et al., 2016). First rheometry measurements with a gold-plated spacecraft model of JUICE have also been performed by us, but more measurements are still needed, and this will be reported in a future paper. Another experimental method of calibration investigates the reception properties of a scale model measured in an anechoic chamber, where the model is directly exposed to radiated electromagnetic waves. Finally, one can use natural radio emissions, like Auroral Kilometric Radiation at Earth or HOM at Jupiter, received by the antennas and receivers on the real spacecraft. From the received signals and the known source location and wave polarization of the emissions one can infer the antenna reception properties. This method is called in-flight calibration and has been done, e.g., for Cassini at Jupiter (Cecconi & Zarka, 2005; Vogl et al., 2004), Interball at Earth (Panchenko, 2004), and STEREO at Earth (Panchenko et al., 2014).

In general, the numerical simulations have provided largely consistent results with the experimental methods and the in-flight calibration. Numerical computer simulations were performed for many spacecraft, for example, Cassini (Fischer et al., 2001; Rief, 2013), Mars Express (Macher et al., 2006), STEREO (Macher et al., 2007; Oswald et al., 2006, 2009; Rucker et al., 2005), Resonance (Sampl et al., 2012, 2015), Solar Orbiter (Sampl et al., 2011), and Juno (Sampl et al., 2016). Numerical simulations are usually cheaper and more

flexible than experimental methods. No metallic "hardware" model needs to be constructed, and one can easily make modifications of the configuration and include rotatable parts in a virtual "software" model in the computer. Furthermore, one can include antenna base capacitances and calculate the antenna reception properties also at higher frequencies, whereas the method of rheometry is restricted to the so-called quasi-static frequencies, for which the wavelength is much larger than the dimension of the spacecraft.

In this paper we report the results from numerical computer simulations for the RWI antennas of the JUICE spacecraft. In Section 2 we will further go into the details of the numerical method and show the mathematical definition of the so-called effective length vector, which is commonly used for the description of the antenna reception properties. In Section 3 our computer model of JUICE will be described in more detail, including the used coordinate system and the antenna naming convention. Section 4 will lay down the main results, and we will show the surface current distribution, the antenna impedances, and the effective lengths vectors for open and loaded ports at quasi-static frequencies. Furthermore, the influence of the solar panel rotation on the effective antenna's reception properties will be studied. Section 5 deals with the antenna reception properties at higher frequencies up to 45 MHz, and we will show many antenna directivity patterns at various frequencies. In Section 6 we will use the numerical simulation to estimate the influence of electric field pulses from other instruments like the active radar of JUICE on the passive RPWI sensors. The final Section 7 will contain some discussion and conclusions.

2. Numerical Methods for Antenna Calibration

2.1. Calculation of Surface Currents and Effective Length Vectors

The reception properties of space-borne radio antennas are often described by the so-called "effective length vector" (Macher et al., 2007; Sinclair, 1950). This concept describes the far-field radiation or reception characteristics, and usually the effective length vector does not coincide with the orientation and length of the corresponding mechanical antenna. It can be calculated by integrating the surface currents on the conductive spacecraft body and antennas in transmission mode. The antenna reciprocity theorem ensures that an antenna's radiation and reception pattern are identical in a linear medium. Large conducting objects in close vicinity of an antenna can alter its electric behavior significantly, especially when the antenna is driven as a monopole, but also dipoles can be influenced. Since the conducting spacecraft body perturbs the antenna pattern, the antenna accommodation crucially determines the reception properties. Assuming that the surface of the spacecraft is a perfect electric conductor, the method of moments (Harrington, 1968) can be used to find the current distribution on the spacecraft by solving the electrical field integral equation:

$$\vec{E} = -\frac{1}{4\pi}\int_S \left[\vec{J_S}(\vec{r'})\cdot\left(\frac{1}{j\omega\epsilon}\nabla'\nabla' - j\omega\mu\right)\right] G(\vec{r},\ \vec{r'})dS' \tag{1}$$

where $\vec{J_S}$ is the surface current of the patch-grid model at the position $\vec{r'}$, $G(\vec{r},\vec{r'}) = \exp(-jkR)/R$ with $R = |\vec{r} - \vec{r'}|$ is the scalar Green's function and $\vec{E}$ is the incident electric field. Furthermore, $j = \sqrt{-1}$ is the imaginary unit, ω is the circular wave frequency, k is the magnitude of the wave vector, μ is the magnetic permeability, ϵ is the permittivity, and the integration is performed over the surface S. Here and in the following the dot $\cdot$ between two quantities means the product with summation over the adjacent indices, in particular a scalar product or a matrix multiplication. Knowledge of the surface currents allows the calculation of the effective length vector for each antenna. For a known current distribution, the effective length vector $\vec{h_e}$ can be calculated with

$$\vec{h_e} = \frac{1}{I_a}\int \vec{J_S}(\vec{r'})\exp(j\vec{k}\cdot\vec{r'})dS' \tag{2}$$

in which the current density $\vec{J_S}$ is integrated over the entire surface of the spacecraft. The current at the antenna terminal is denoted by I_a, and $\vec{k}$ is the propagation vector of the received plane wave. If the vector potential $\vec{A}(\vec{r})$ at an observation point $\vec{r}$ in the far-field can be determined in transmission mode (antenna driven by current I_a), $\vec{h_e}$ can also be calculated by inversion of the following equation:

$$\vec{A}(\vec{r}) = \frac{\mu}{4\pi}\frac{\exp(-j\vec{k}\cdot\vec{r})}{r} I_a\vec{h_e} \tag{3}$$

Equation 2 shows that the effective length vector $\vec{h_e}$ depends on the wave vector $\vec{k}$, which means that it depends on the direction of the incoming radio wave as well as its wavelength. For the so-called "quasi-static" case Equation 2 simplifies considerably, since we can set $\exp(j\vec{k}\cdot\vec{r'}) = 1$. This approximation is possible for $|\vec{k}\cdot\vec{r'}| \ll 1$, which implies radio waves with a long wavelength compared to the size of the spacecraft. As long as the wavelength is much larger than the spacecraft dimensions (i.e., case of short antennas), the effective length vector is a real constant vector (with an insignificant imaginary part) pointing into the direction of the minimum gain in the antenna reception pattern. In our case with spacecraft dimensions of a few meters this is mostly fulfilled at frequencies below ~ 1 MHz, which is called the "quasi-static" frequency range. Above this range the effective length vector is a complex quantity which depends on the frequency and on the direction of the incoming radio wave as Equation 2 shows. The open-circuit voltages V_i at each antenna i can be expressed as

$$V_i = \vec{h_i}\cdot\vec{E} \tag{4}$$

where $\vec{h_i}$ is an effective antenna length vector, $\vec{E}$ is the electric wave vector of the incoming wave and i denotes the antenna. Each $\vec{h_i}$ vector can be represented by Cartesian coordinates $\vec{h_i} = (h_{i,x}, h_{i,y}, h_{i,z})$ or by the spherical coordinates of antenna length h_i, colatitude θ_i, and azimuth ϕ_i. The effective length vector of the antenna represents the electrically effective direction and length of each antenna, in contrast to the physical (mechanical) antenna.

2.2. Transfer Matrix Representation of Antenna Systems

For the effective length vector one needs to distinguish between open and loaded ports. The so-called open port effective length vector represents the reception properties of the bare antenna system. It does not take the loads into account which have a large influence on the measured voltages. The loads are composed of receiver input impedances, cable capacitances, and eventual capacitances of the mounting zones. The mounting capacitances are to be included in the loads if the mountings are not represented in the model. Since the operational frequency we are interested in is very low, the load is practically capacitive, and we call it "base capacitance." Generally, the loads at the ports can be represented by a local impedance matrix $\mathbf{Z_L}$. The effect of loaded ports on the so-called transfer matrix $\mathbf{T}$ is given by (Macher, 2008, 2012; Macher et al., 2007)

$$\mathbf{T} = (\mathbf{1} + \mathbf{Z_A}\cdot\mathbf{Z_L^{-1}})^{-1}\cdot\mathbf{T^o} = (\mathbf{1} + \mathbf{C_A^{-1}}\cdot\mathbf{C_L})^{-1}\cdot\mathbf{T^o} \tag{5}$$

where $\mathbf{Z_A}$ and $\mathbf{C_A}$ are the antenna impedance and capacitance matrices, and $\mathbf{T^o}$ is the open port transfer matrix which contains the open port effective length vectors as rows. Note that the bold print in the previous equation represents matrices, and $\mathbf{1}$ is the identity matrix. The second equality is valid in the quasi-static frequency range in which the antenna and load impedances are mainly capacitive with a resistivity close to zero. The load capacitance matrix $\mathbf{C_L}$ contains the base capacitances in its main diagonal, and the off-diagonal elements are the mutual capacitances, which are practically zero. Mutual capacitances can be present in the antenna capacitance $\mathbf{C_A}$, but they are typically two orders of magnitude smaller than the capacitance values of the main diagonal. In the case of the three RWI antennas, the open port effective transfer matrix $\mathbf{T^o}$ can be written in the following way

$$\mathbf{T^o} = \begin{pmatrix} h^o_{U,x} & h^o_{U,y} & h^o_{U,z} \\ h^o_{V,x} & h^o_{V,y} & h^o_{V,z} \\ h^o_{W,x} & h^o_{W,y} & h^o_{W,z} \end{pmatrix} \tag{6}$$

with U, V, W as the names of the antennas and x, y, z as the respective Cartesian coordinate. The superscript "o" refers to the open port. The 3 × 3 transfer matrix $\mathbf{T}$ is related to the column voltage vector

$\overrightarrow{V} = (V_U, V_V, V_W)$ (voltages at U, V, W dipole) and the electric field column vector $\overrightarrow{E} = (E_x, E_y, E_z)$ via the well-known equation (Macher et al., 2007)

$$-\overrightarrow{V} = \mathbf{T} \cdot \overrightarrow{E}. \tag{7}$$

We applied the computational electromagnetic software FEKO (FEldberechnung für Körper mit beliebiger Oberfläche; German expression for calculation of fields for bodies with arbitrary surfaces), which is a highly sophisticated commercial antenna simulation tool based on the solution of the electric field integral equation. The current distribution on the antenna-spacecraft system was calculated with the Method of Moments in double precision by FEKO. Then it was used to retrieve antenna properties such as radiation patterns, effective antenna vectors using Equation 2, and antenna impedances. For the latter calculations we utilized our in-house MATLAB antenna toolbox library developed at the Space Research Institute of the Austrian Academy of Sciences.

2.3. The Usage of a Calibrated Antenna System

With a calibrated antenna system of three antennas it is possible to retrieve the intensity, polarization, and incoming wave direction of a radio wave. These quantities are physically described by the four Stokes parameters S, Q, U, V (see, e.g., Kraus, 1966 or Carozzi et al., 2000) and by two angles of incidence, that is, by a total of six quantities. The basic Equations 4 or 7 relate the output voltages at the antennas to the electric field $\overrightarrow{E}$ of the incoming radio wave, and they are obviously related by the effective antenna vectors or transfer matrix, which we determine in this paper. The receiver measures quantities such as $\langle V_n V_k^* \rangle$, which are the time-averaged correlations between the voltages at antennas n and k. The RWI receiver will be able to measure nine different quantities, which are the three auto-correlations ($\langle V_U V_U^* \rangle$, $\langle V_V V_V^* \rangle$, $\langle V_W V_W^* \rangle$), the three real parts of the cross-correlations ($\Re(\langle V_U V_V^* \rangle)$, $\Re(\langle V_U V_W^* \rangle)$, $\Re(\langle V_V V_W^* \rangle)$), and the three imaginary parts of the cross-correlations ($\Im(\langle V_U V_V^* \rangle)$, $\Im(\langle V_U V_W^* \rangle)$, $\Im(\langle V_V V_W^* \rangle)$). These nine measured quantities provide an overdetermined equation system for the determination of the mentioned six unknowns, a solution of which can be obtained by appropriate least squares fits. To further improve the accuracy and condition of the equation system, observations under different antenna/spacecraft orientations with regard to the source positions are evaluated. How this can be achieved in detail is described by Ladreiter et al. (1995), Vogl et al. (2004), and Cecconi and Zarka (2005). The last two references contain more specific information on the application to Cassini RPWS (Radio and Plasma Wave Science instrument). The articles also emphasize that without accurate knowledge of the antenna reception properties it is not possible to reliably determine intensity, polarization, and incidence direction of observed radio waves from the recorded signals.

3. The Model of JUICE

3.1. Description of JUICE Model and Its Coordinate System

The numerical simulations of the JUICE/RWI antennas are based on a patch grid model of the whole spacecraft including the most essential features. We used a very detailed CAD model of the spacecraft which we obtained from Airbus. This original CAD model consisted of a great amount of details which were not necessary for our simulations. Increasing the level of details represented in the model improves the results up to a maximum degree of accuracy. However, a further refinement would introduce numerical rounding errors which outweigh the gained model accuracy. Also, very complex models need extremely long calculation times. Therefore we have built a reduced model where many fine structures have been either removed or simplified. Additionally, all internal parts below the conductive surface are irrelevant for the calculations and were removed as well. The spacecraft surface was assumed to be a perfect electrical conductor, as using highly conductive surface materials where possible was the standard technique applied to JUICE to avoid arcing and other negative effects of spacecraft charging. The surrounding medium was assumed to be vacuum. The RWI antenna signals are processed by the high frequency receiver only above the frequency of 80 kHz, which is high above the plasma frequency in most regions of the Jovian magnetosphere (Gurnett et al., 1981). Just near the Galilean icy moons the electron plasma frequency is expected to rise to a few hundred kHz.

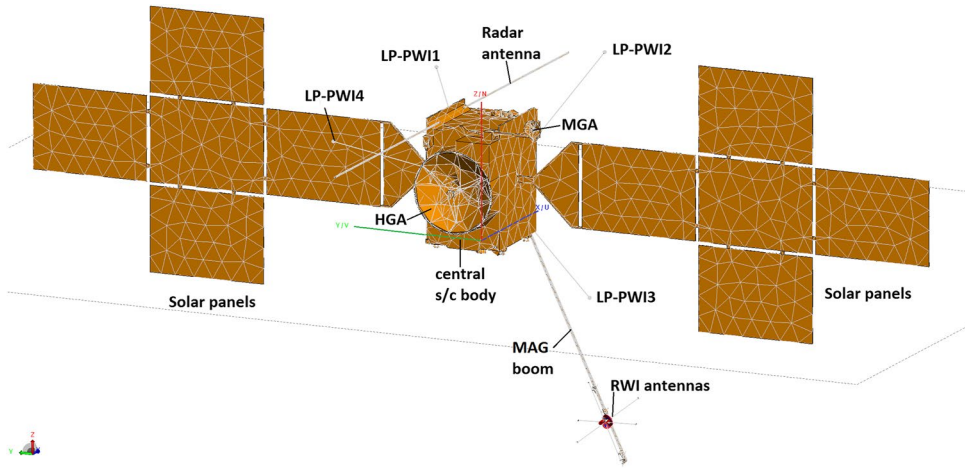


Figure 1. Mesh model of the Jupiter Icy Moons Explorer spacecraft used for numerical computer simulation with main spacecraft parts being annotated.

Our model was prepared with the CAD program Solid Edge, and it was imported as Parasolid file into the so-called CADFEKO tool, which is used to construct a mesh model for FEKO. The final mesh model consisted of about 25,000 triangles, and it can be seen in Figure 1.The spacecraft structures which are most important with regard to the antenna properties are the central spacecraft body, the HGA (High Gain Antenna), the MGA (Medium Gain Antenna), the large solar panels (SP), the Langmuir probes LP-PWI1-LP-PWI4, the radar antenna, and the magnetometer (MAG) boom with the RWI antenna triad. The origin of the used Cartesian coordinate system is located at the bottom of the central spacecraft body, and in Figure 1 the x, y, and z axes are drawn in blue, green, and red color, respectively. The positive x-axis points opposite to the HGA direction, the y-axis direction is along the SP (with the negative side where the MGA is located), and the z-axis completes the orthogonal, right-handed triad. Each position or vector can also be described in spherical coordinates with θ as the co-latitude, ϕ as the azimuth, and r as the radius.

The central spacecraft body is roughly a cuboid with sizes of 2.6 × 2.2 × 3.6 m in x, y, and z direction, respectively. The HGA dish has a diameter of ∼2.4 m and is pointing into the −x direction. The MGA dish has a diameter of ∼0.5 m, and it is looking into the same direction as the HGA. It is mounted on a ∼1.4 m long boom in −y direction with a foot point on the upper deck of the central body. In the model the SP consists of 2 wings with 5 rectangles on each side with a size of about 2.5 × 3.5 m. This gives a total area of ∼87.5 m^2. We note that the initial size of the SP was larger, about 2.5 × 4.0 m for each of the 10 sub-panels. There are four spherical LP with a diameter of 10 cm each, and each of them is located on a ∼3.2 m long boom. The booms are mounted on the central spacecraft body, and in Figure 1 they can be seen as gray lines, with three of them sticking out in a tilted way from the +x side of the central body. The fourth one has its foot point close to the HGA on the −x side, and this one is a bit shorter, just ∼3.0 m long. The radar antenna of the RIME instrument (Radar for Icy Moons Exploration) is a dipole situated at the upper deck of the central body and oriented along the x-direction. Its tip-to-tip length is 16 m. Finally, the MAG boom was modeled as a 10.6 m long boom with a diameter of 8 cm. It is located parallel to the xz-plane at $y = -0.83$ m, and it has an angle of 141° with respect to the $+z$ direction.

3.2. The RWI Antennas and Their Naming Convention

The RWI antenna triad is located at a distance of ∼8.5 m from the foot point of the MAG boom. The left panel of Figure 2 shows a photo of the real RWI antenna system, in which the three dipoles are mounted on top of a cubic box which contains the pre-amplifiers (hidden below a multi-layer insulation). The RWI system is displayed in stowed configuration with the antennas rolled up on storage reels. The antennas are named U, V, and W in such a way that U+, V+, and W+ form a right-handed system. The positive dipole arms (U+, V+, W+) are directed towards the side of the interface plate with the MAG boom below the cubic pre-amplifier box. The three dipole antennas are perpendicular to each other, and the tip-to-tip length

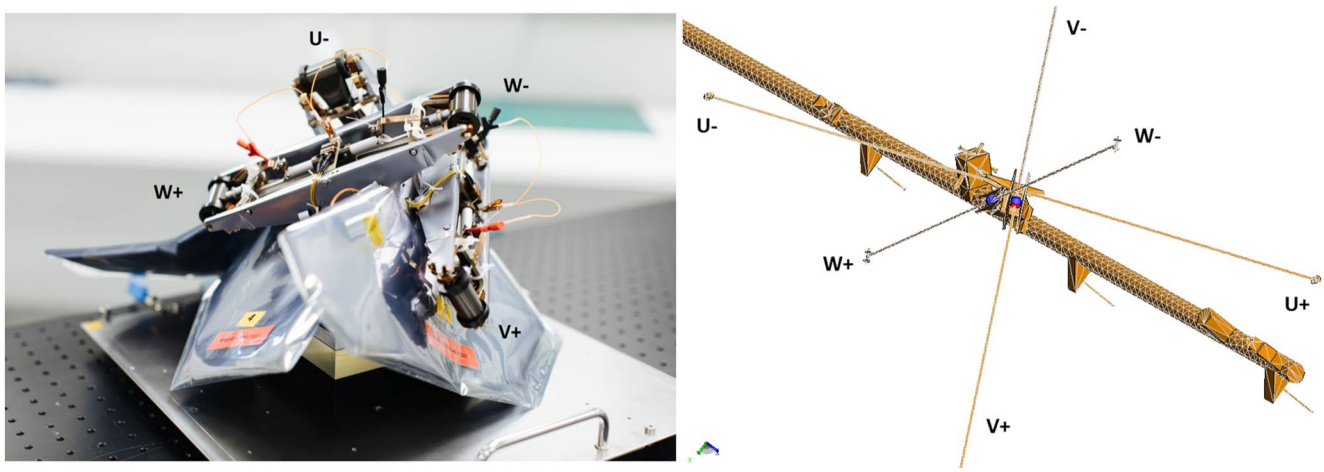


Figure 2. The left panel shows the real Radio Wave Instrument (RWI) flight model in stowed configuration. The three dipoles are rolled up, and the names of the dipole arms are indicated. The positive arms U+, V+, W+ point towards the side of the interface plate with the MAG boom at the bottom. The right panel shows a detailed view of the RWI antenna system in our Jupiter Icy Moons Explorer mesh model. The dipoles are orthogonal to each other and have their central feeding points right above the cubic pre-amplifier box.

of each dipole is 2.5 m. The antennas were built from beryllium copper tape springs, and after deployment they have the form of a tube with a diameter of 1 cm. The right panel of Figure 2 shows how the RWI antenna system has been modeled in our JUICE spacecraft model, and the names of the antennas are annotated. The other box on the left side behind the RWI (this is the direction towards the spacecraft body) is the SCM of the RPWI instrument. The antenna feeds are located at the central points of each antenna, right above the pre-amplifier box. So the dipoles are center-fed, and each dipole arm has a length of 1.25 m. The MAG boom has a cylindrical shape with a diameter of 8 cm, and the circular cross-section of this cylinder is turned into an octagonal cross-section in the mesh model.

Table 1 gives the exact location of the antennas and the MAG boom in the spacecraft coordinate system. The first numbers represents the Cartesian coordinates x, y, z of the tips of the positive dipole arms (U+, V+, W+), and the second numbers are the coordinates of the negative dipole arm tips (U−, V−, W−). Additionally, each antenna vector is also given in spherical coordinates, and the orientation of the antenna vector is defined as pointing from the negative dipole arm towards the positive one. For the MAG boom the first numbers of the Cartesian coordinates are those from the base, and the second numbers are the coordinates of the boom's tip, and the vector points from the base to the tip. One can see in Table 1 that the z coordinates of the positive tips of U+ and W+ are larger than the z coordinates of the negative dipole arm tips of U− and W−. This was one reason to call those dipole arms the positive ones since they are pointing towards the $+z$ direction. However, this is not the case for the V-dipole.

Table 1
Radio Wave Instrument Antenna Positions and MAG Boom in the Spacecraft Coordinate Frame

	Cartesian coordinates			Spherical coordinates		
Antenna name	X [m]	Y [m]	Z [m]	h [m]	θ [deg]	ϕ [deg]
U + U−	[7.703, 5.525]	[−1.340, −0.456]	[−6.146, −7.022]	2.5	69.6	−22.1
V + V−	[7.189, 6.134]	[0.269, −1.979]	[−6.834, −6.481]	2.5	98.1	64.9
W + W−	[6.254, 6.914]	[−0.474, −1.149]	[−5.456, −7.780]	2.5	22.1	134.4
Boom	[1.317, 7.988]	[−0.830, −0.830]	[0.172, −8.066]	10.6	141.0	0.0

Note. The First Column Gives the Name of the Antenna or the Boom. Columns 2–4 give the Cartesian coordinates of the tips of U+, V+, W+ followed by the tips of U−, V−, W−. Columns 5–7 give the spherical coordinates (length h, colatitude θ, azimuth ϕ) of each dipole or the boom. For the MAG boom the Cartesian coordinates go from the base to the tip point.

3.3. Development of the RWI Antenna System

To perform radio wave direction-finding (goniopolarimetry) it is required that measurements of auto- and cross-correlations are done for at least three antennas. The three antennas should not have three co-planar effective length vectors, and it is required that the angular separation of the three effective antenna length vectors is large, that is, angles larger than 70° are preferred. If that is not the case and effective antenna vectors are not sufficiently spatially separated, the accuracy of radio wave direction-finding is deteriorated (Cecconi & Zarka, 2005). Radio wave direction-finding, polarization and intensity measurements are major scientific objectives of RPWI within the JUICE mission. They all require a calibrated antenna system.

Before we start with the presentation of the calibration results in the next section, we give a short overview how the JUICE RWI antenna system was developed in recent years. The initial RWI baseline configuration was different, and it had three short RWI monopole antennas mounted on the large spacecraft body. Using numerical computer simulations it was found that such a configuration (three short monopole antennas on a large spacecraft) leads to an insufficient angular separation between the three effective lengths vectors, which would degrade the quality of the scientific data (Fischer et al., 2017). Hence, the baseline configuration was changed to three dipoles mounted on the magnetometer boom.

Here we only mention briefly that we did several numerical simulations with the aim to find the orientation of the RWI dipoles on the MAG boom with the optimal reception properties. Our models with the three dipoles on the boom were also varied in many ways (e.g., attitude of antenna triad, position of feed points, distance of dipoles to boom, boom length and diameter, antenna diameter) to get a physical understanding which parameters mostly influence the directions and lengths of the effective length vectors. It turned out that the exact position of the feed point with respect to the boom is a crucial parameter, where little changes can lead to large changes in the antenna characteristics. As mentioned above, it is required that all three effective length vectors of the dipoles should not get too short and should have a sufficient angular separation ($> 70°$ and $< 110°$) from each other.

After these test calculations we ran ~37,000 numerical simulations of a simplified, small model with different antenna attitudes in a systematic way (with a genetic algorithm) to find the optimum configuration with the best antenna reception properties. To save calculation time, the simplified model consisted of only ~1300 triangles, and was far less detailed as the model shown in Figure 1. In this process the RWI antenna system was modeled as constructed (and shown in Figure 2) with three orthogonal antennas placed on the cubic pre-amplifier box. Five different parameters were varied in this optimization process, namely three angles describing the orientation of the whole RWI antenna triad, and two distances, namely the vertical and lateral shift of the whole RWI antenna system with respect to the MAG boom. The optimization criteria were to come close to orthogonality also for the three effective antenna vectors, to achieve maxima in effective lengths, and to avoid antennas pointing close to the $+z$-direction, because this is the direction into which most instruments are pointing and therefore should often also be the direction of incidence of Jovian radio emissions. The result of this optimization process are the dipole positions given in Table 1. For this configuration the orthogonal RWI antenna triad as displayed on the left side in Figure 2 could not be mounted directly onto the MAG boom, so it was necessary to include an orientation bracket between the MAG boom and the plate at the bottom of the cubic pre-amplifier box.

4. Calibration Results for Open and Loaded Ports

4.1. Current Distribution, Antenna Capacitance, and Transfer Matrix for Open and Loaded Ports

Figure 3 shows the current distribution on the surface of JUICE for a quasi-static frequency of 300 kHz, which was calculated for an excitation of 1 Volt using the program package FEKO. The upper plot shows small line current densities of around -180 dB A m^{-1} (1 nA m^{-1}) on the outer SP and parts of the spacecraft body, and around -120 dB A m^{-1} (1 μA m^{-1}) on parts of the spacecraft and the MAG boom. Around the excitation zone, which is the V-dipole in this case, the densities are even higher than -60 dB A m^{-1} (1 mA m^{-1}) as the lower panel of Figure 3 shows.

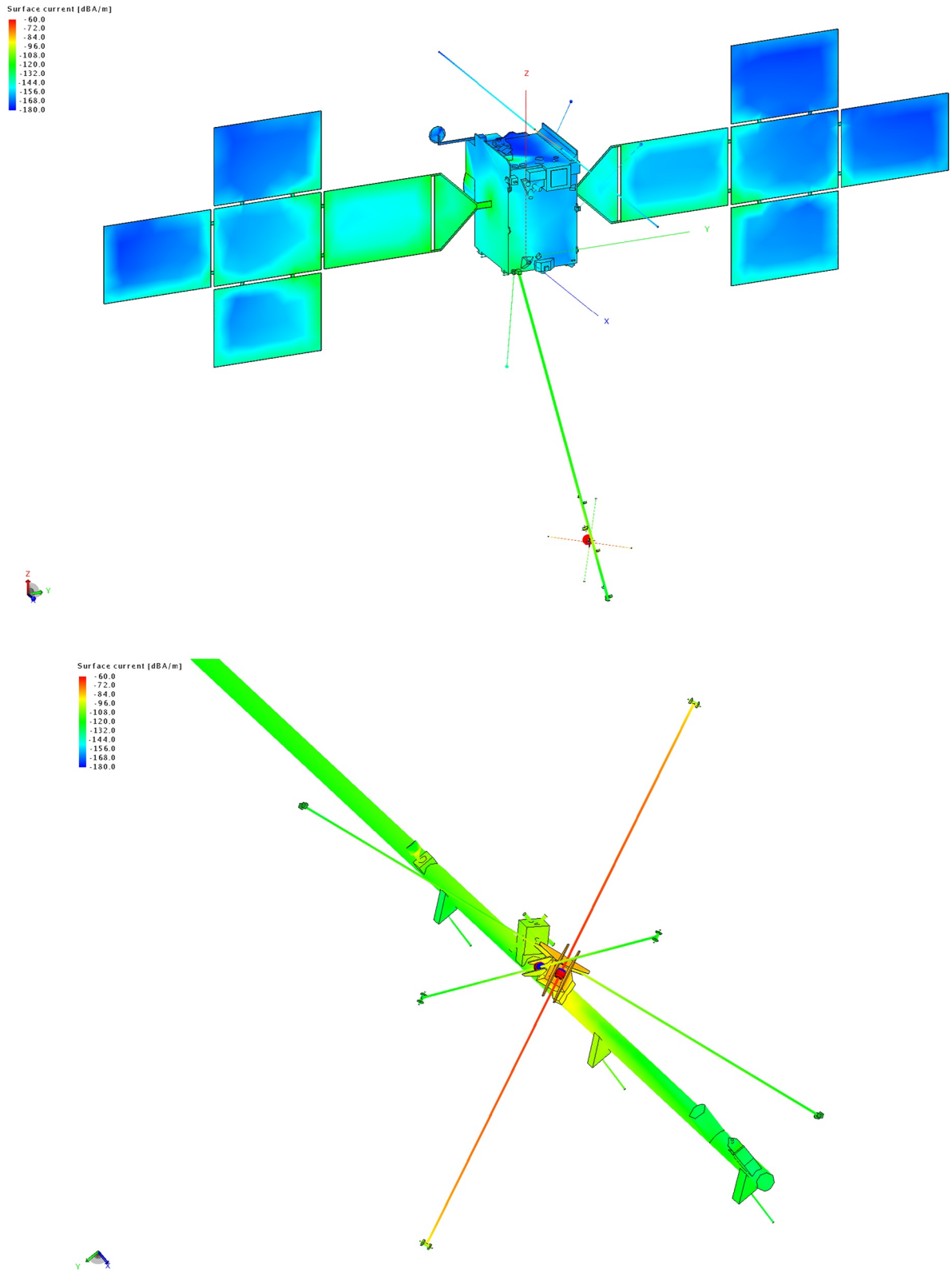


Figure 3. Surface currents (dB A m^{-1}) for the JUICE-RWI model with dipole V driven with 1 Volt at 300 kHz. The color scale goes over six orders of magnitude from −60 to −180 dB A m^{-1}, which corresponds to 10^{-3} A m^{-1} to 10^{-9} A m^{-1}.

Table 2
Open Port and Loaded Port Effective Length Vectors in Comparison for U, V, and W Dipole.

	Open ports			Loaded ports (25 pF)			Loaded ports (45 pF)		
Antenna name	h^o [m]	θ^o [deg]	ϕ^o [deg]	h^l [m]	θ^l [deg]	ϕ^l [deg]	h^l [m]	θ^l [deg]	ϕ^l [deg]
U + U−	1.07	44.6	−25.7	0.26	45.1	−25.9	0.17	45.1	−25.9
V + V−	0.92	85.4	72.5	0.23	84.8	73.1	0.14	84.8	73.1
W + W−	1.87	27.6	156.3	0.48	27.7	155.9	0.30	27.7	155.8

Note. For the loaded port, base capacitances of 25 and 45 pF were taken. The letter h denotes the effective length, the angle θ is the colatitude, and ϕ is the azimuth. The superscripts "o" and "l' denote the values for open ports and loaded ports, respectively.

The knowledge of the voltage and current at the antenna port can be used to calculate the antenna impedance, which practically is only capacitive in the quasi-static frequency case (Macher et al., 2007). The antenna capacitance matrix at 300 kHz was calculated to be

$$\mathbf{C_A}[pF] = \begin{pmatrix} 8.259 & -0.034 & -0.046 \\ -0.032 & 8.249 & 0.081 \\ -0.044 & 0.084 & 8.665 \end{pmatrix} \tag{8}$$

It can be seen that the self-capacitances on the main diagonal are around 8–9 pF, whereas the mutual capacitances are a factor of ∼100 smaller. The antenna capacitance for a cylindrical dipole arm can be estimated with the following formula (Jackson, 1975):

$$C_a = \frac{2\pi\epsilon_0 l_a}{[\ln(\frac{l_a}{a}) - 1]} \tag{9}$$

with l_a as the length of one dipole arm, a as the antenna radius, and ϵ_0 as the permittivity of free space. Using the geometrical values for one RWI dipole arm (l_a = 1.25 m and a = 0.5 cm) we obtain $C_a \sim 15.4$ pF as the capacitance of one dipole arm (monopole) versus infinity. Since the full dipole can be represented as the two capacitances of each dipole arm in series, the antenna capacitance of the dipole is indeed half of the capacitance of the monopole arm, that is, for the RWI dipole we have $C_A = C_a/2 \sim 7.7$ pF. It can be seen that this estimation is just a bit smaller than our calculated result around 8–9 pF. The reason for this is that the estimate ignores the stray capacitance associated with the electric field in the gap between the terminals of the antenna, which induces charge separation in the conducting parts of the mounting structure, leading to additional charging of the dipole arms.

We now give the results for the effective length vector, which also can be given in the form of a so-called "transfer matrix". The open port transfer matrix $\mathbf{T^o}$ is given by the Cartesian coordinates of the three effective length vectors (U, V, W) of the RWI antenna system as rows of the following matrix:

$$\mathbf{T^o}[m] = \begin{pmatrix} 0.677 & -0.325 & 0.760 \\ 0.276 & 0.876 & 0.073 \\ -0.791 & 0.347 & 1.656 \end{pmatrix} \tag{10}$$

The spherical coordinates of these three vectors can be found in Table 2. For the calculation of the transfer matrix for loaded ports we use Equation 5 given by

$$\mathbf{T} = (\mathbf{1} + \mathbf{C}_\mathbf{A}^{-1} \cdot \mathbf{C}_\mathbf{L})^{-1} \cdot \mathbf{T}^\mathbf{o} = \begin{pmatrix} 0.169 & -0.082 & 0.187 \\ 0.067 & 0.218 & 0.021 \\ -0.204 & 0.091 & 0.426 \end{pmatrix} \quad (11)$$

The antenna capacitance is given by Equation 8, the open port transfer matrix $\mathbf{T}^\mathbf{o}$ is given by Equation 10, and the load capacitance is $\mathbf{C}_\mathbf{L} = \mathbf{1} \times 25$ pF, which is the identity matrix times 25 pF. The spherical coordinates of the transfer matrix $\mathbf{T}$ with loaded ports is also given in Table 2. We also used a base capacitance of 45 pF due to some uncertainties in the base capacitance measurement, but 25 pF is the most probable value and 45 pF should be the maximum. The results show that the effective dipole axes are scarcely changed by the modification of the base capacitance, whereas the effective length undergoes the expected considerable shortening when the base capacitance is increased.

A quick look on the results in Table 2 also shows that the effective length of the W-dipole is about twice that of the U or V-dipole. This is probably due to a difference in coupling between the respective antenna and the close MAG boom caused by different angular distances between each antenna and the boom. The angular separation between the W-dipole and the MAG boom is ~28°, whereas the angles between the U-dipole/V-dipole and the MAG boom are ~74° and ~68°, respectively. The angle between the effective length vector of the W-antenna and the MAG boom is just ~17°, which means that the radiation coupling with the spacecraft pushes the effective axis of the W-antenna towards the boom. Usually objects near the antenna arms have the opposite effect, that is, pushing the effective antenna axes away. In fact, this occurs for the U and V antenna as the effective U and V axes are almost orthogonal to the boom, that is, those angles are ~81° and ~ 83°, respectively (all angles measured for the case of open ports). So the W antenna behaves significantly different in this respect. The reason is the influence of the large spacecraft and SP in connection with the boom. It can be interpreted in terms of Equation 2, which gives the dependence of the effective length vector on the currents through the whole model (antenna, SP, boom, etc.) when driven by a current I_a at transmission. For frequencies below the full-wave resonance the time-dependent AC current charges the two antenna arms of a dipole with opposite signs, alternating with the given frequency. Due to radiation coupling (in the quasistatic range simply the attraction of opposite charges) a charge separation is occurring in the nearby boom in such a way that negative charges appear in boom parts close to the positively charged antenna arm, and vice versa. So a current flow I' is induced in the boom counteracting the current in the antenna, reducing the result of the summation in Equation 2. The effect is also that the contribution of the boom currents in the vectorial sum leads to a larger angle between the effective antenna and the boom. This is exactly what happens with the U and V dipole.

The influence of the spacecraft with its large SP could be analyzed in analogous fashion if they were not connected to the boom. However, the connection of the spacecraft with the boom makes a great difference. It allows a charge separation between them, which means that a negative charge from the spacecraft may be attracted towards the boom where the dipoles are mounted. Since the U and V dipole enclose a large angle with the boom, this effect is negligible for them: both arms of each, U and V, have almost the same distance from the spacecraft and the panels, and so the attraction by the oppositely charged arms cancel. The situation is different for the W dipole. If its arm W+, which is closer to the spacecraft than W−, is positively charged, negative charges from the spacecraft are attracted towards the boom (collecting on the boom between the spacecraft and the W+ tip). This results in a current I'' with the same orientation as the current on the W dipole! Of course, there is still the induced opposite current I' on the boom part around the W feed zone, for the same reasons as explained above for U and V. Due to the big area of the SP, the contribution of I'' in Equation 2 exceeds the contribution of I'. In consequence, a larger effective length and an effective axis tilted towards the boom is obtained for W, which is exactly opposite to the effect on U and V.

It is interesting to note that for a radio wave coming from the $+z$-direction (e.g., JUICE in nadir-pointing facing Jupiter) the effective lengths of all three antennas are relatively similar. This is due to the fact that a free space electromagnetic wave incident from the $+z$ direction does not have a z-component, and therefore

Table 3
Loaded Port (25 pF) Effective Length Vectors for U, V, and W Dipole for Various Solar Panel Positions Indicated on the Top of Each Column

	− 75°			− 60°			− 45°		
Antenna name	h^l [m]	θ^l [deg]	ϕ^l [deg]	h^l [m]	θ^l [deg]	ϕ^l [deg]	h^l [m]	θ^l [deg]	ϕ^l [deg]
U + U−	0.27	44.2	−25.8	0.27	44.4	−25.6	0.27	44.7	−25.4
V + V−	0.23	84.3	72.8	0.23	84.4	72.6	0.23	84.5	72.5
W + W−	0.48	27.4	155.7	0.48	27.3	155.7	0.48	27.4	155.7
	− 30°			− 15°			0°		
Antenna name	h^l [m]	θ^l [deg]	ϕ^l [deg]	h^l [m]	θ^l [deg]	ϕ^l [deg]	h^l [m]	θ^l [deg]	ϕ^l [deg]
U + U−	0.27	44.9	−25.4	0.27	45.0	−25.6	0.26	45.1	−25.9
V + V−	0.23	84.7	72.6	0.23	84.8	72.8	0.23	84.8	73.1
W + W−	0.48	27.5	155.8	0.48	27.6	155.8	0.48	27.7	155.9
	+ 15°			+ 30°			+ 45°		
Antenna name	h^l [m]	θ^l [deg]	ϕ^l [deg]	h^l [m]	θ^l [deg]	ϕ^l [deg]	h^l [m]	θ^l [deg]	ϕ^l [deg]
U + U−	0.26	44.9	−26.1	0.26	44.8	−26.3	0.26	44.5	−26.4
V + V−	0.23	84.8	73.3	0.23	84.7	73.4	0.23	84.5	73.4
W + W−	0.48	27.8	155.9	0.48	27.8	155.8	0.48	27.7	155.8
	+ 60°			+ 75°			+ 90°		
Antenna name	h^l [m]	θ^l [deg]	ϕ^l [deg]	h^l [m]	θ^l [deg]	ϕ^l [deg]	h^l [m]	θ^l [deg]	ϕ^l [deg]
U + U−	0.26	44.3	−26.4	0.27	44.2	−26.2	0.27	44.2	−26.0
V + V−	0.23	84.4	73.4	0.23	84.3	73.2	0.23	84.3	73.0
W + W−	0.48	27.7	155.7	0.48	27.5	155.7	0.48	27.4	155.7

Note. The letter h denotes the effective length, the angle θ is the colatitude, and ϕ is the azimuth.

it is the projection of the effective length vector into the xy-plane which is relevant. And this projection has a length of ∼0.8 m for open ports and ∼0.2 m for loaded ports of 25 pF. This can easily be calculated from Equations 10 and 11 by using only the x and y-components of the transfer matrix. The large effective length of the W-antenna mostly comes from its z-component.

4.2. Results for Different Orientations of the Solar Panels

We have also simulated the antenna reception properties of the rotatable SP, which due to their size should also have a certain influence on the effective antenna directions. The panels can be turned by ±90° out of the vertical position during different phases of the mission. We define the vertical position of 0° as the one displayed in Figure 1, where the panels are located in the yz-plane at x = 0. This will be the default and probably the most used position, because here the HGA and the panel's normal are pointing into the same (−x) direction towards Earth and the Sun, which are not that far apart from each other when viewed from Jupiter.

The values of the effective antennas in spherical coordinates can be found in Table 3 for the various solar panel positions. The sign of the solar panel rotation angle is defined in the following way: It is negative when the panels are turned counterclockwise from the vertical position of 0° when viewed by an observer standing on the −y side, and it is positive when the turning is done clockwise. For example, when the angle is –45° the solar panel and the MAG boom are almost coplanar (−), whereas a turn by +45° puts the MAG boom almost perpendicular (+) to the solar panel plane. We note that due to the planar symmetry of the SP in our model a rotation of −90° is equivalent to a rotation of + 90°, whereas for the real spacecraft it will be decisive for its energy management in which way the SP are pointing.

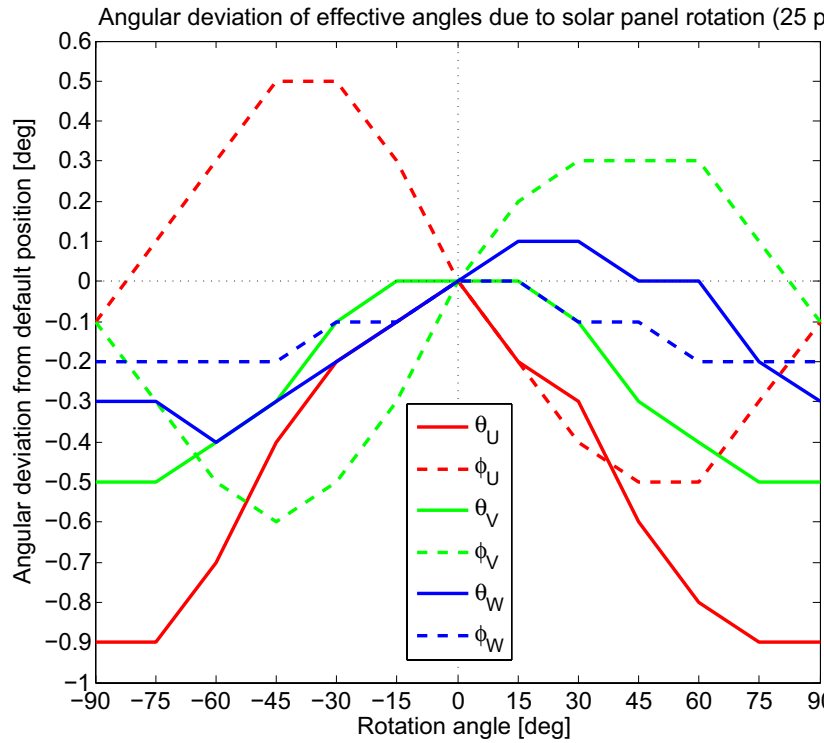


Figure 4. Deviation of effective antenna angles from default position at 0° as a function of solar panel rotation angle. The used model is the one with loaded ports of 25 pF at a quasi-static frequency of 300 kHz. The values for the U-antenna are drawn in red, those for the V-antenna are drawn in green, and those for the W-antenna are drawn in blue. The colatitudes θ are drawn as solid lines, whereas the azimuthal angles ϕ are drawn as dashed lines.

The values in Table 3 were calculated for loaded ports of 25 pF, because this is most likely very close to the real situation. However, using Equation 5 one can easily evaluate them for open ports or loaded ports of any other value. The antenna capacitance $\mathbf{C_A}$ only shows negligible change of the order of 0.01% for different solar panel orientation angles, and so the constant value of Equation 8 can be taken for such a calculation.

Table 3 and Figure 4 show that the typical change of the effective antenna angles is a few tenth of a degree. The change in antenna length is practically negligible and is only 1 cm at most. The deviation of the effective antenna angles from the default position at 0° is drawn in Figure 4, and they were calculated using the values of Table 3. The largest deviations can be seen for the U-antenna, whose colatitude changes by up to −0.9° and whose azimuth varies by ±0.5° around the default position. The minimum deviation appears for the W-antenna with a peak-to-peak variation of just 0.5° for its colatitude and only 0.2° for its azimuth.

5. High Frequency Characteristics

The directivity patterns and the impedances of the antennas have also been simulated up to frequencies of 45 MHz, which is the upper frequency limit of the receiver and of Jovian decametric radio emissions. The simulations in this section were performed with a slightly reduced mesh grid of about 16,000 triangles. This was achieved by modeling the RIME antenna, the four booms of the LP, and some bars at the HGA and MGA not as extended bodies, but as wires with an adapted radius. This reduced the calculation time by about a factor of three (compared to a model with 25,000 triangles) for a single frequency, and this was done as we calculated more than 45 different frequencies. A comparison of the effective antenna angles of the reduced model with the previous model from Sections 3 and 4 at a frequency of 300 kHz revealed only slight differences; the colatitudes and azimuths of the U and V-antenna differed by only 0.1°, and the effective Z-antenna orientation was practically the same.

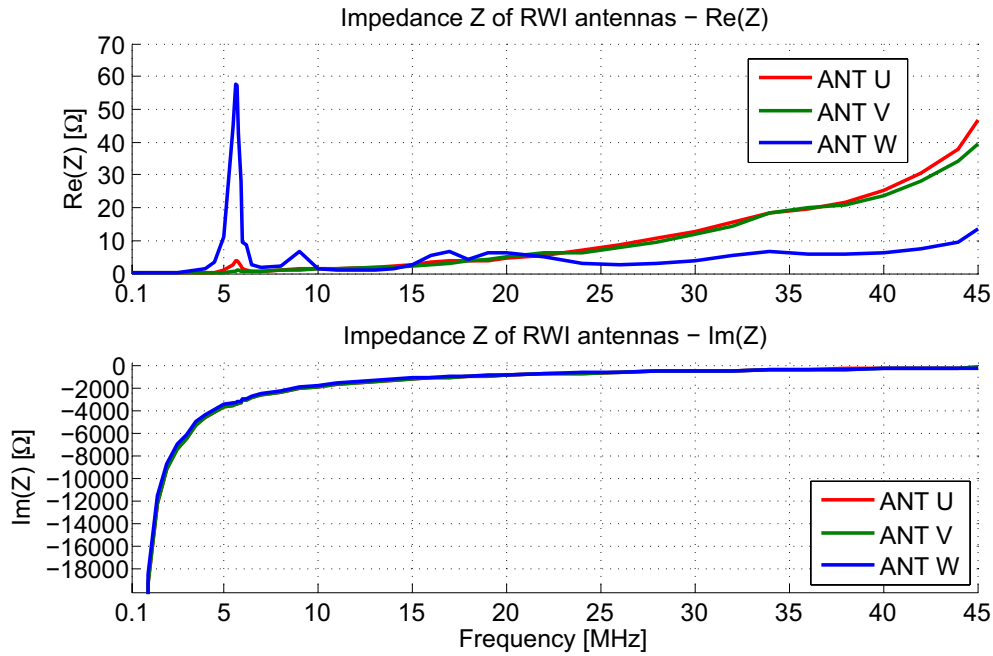


Figure 5. Complex antenna impedances of U, V, and W-dipole as a function of frequency. The upper panel shows the real part, and the lower panel shows the imaginary part of the impedance. The negative imaginary part indicates highly capacitive antennas.

The real and imaginary part of the antenna impedances from 0.1 to 45 MHz of all three RWI dipoles can be seen in the upper and lower panel of Figure 5, respectively. For an antenna tip-to-tip length of 2.5 m the first antenna resonance is at 60 MHz. This corresponds to a wavelength of $\lambda = 5$ m, which is the half wavelength-resonance. This resonance is beyond the display in Figure 5, but one can already see the rise of the impedances for the real part, and the approach of the imaginary part towards the zero-crossing. The real part of the impedance of the W-dipole shows a large resonance around 5.8 MHz, which is less obvious for the U-dipole and nearly absent for the V-dipole. It is most likely caused by the influence of the large SP. Setting $\lambda/2 = 27.6$ m (half wavelength equal to the maximum distance from one end of one solar panel to the other) leads to $\lambda = 55.2$ m and a frequency of $f = 5.4$ MHz. Furthermore, the induced currents also oscillate between the tip of a solar panel and the tip of the MAG boom. This distance is about $12.5 + 2.3 + 10.6 = 25.4$ m, and assuming this distance equals $\lambda/2$, we get $\lambda = 50.8$ m or a frequency of $f = 5.9$ MHz, which is almost identical to the resonance frequency of the W-dipole. Those currents on the MAG boom seem to couple best into the W-dipole, since it is the antenna which is closest to being parallel to the MAG boom (angle of 27.7°). The angles between the U-dipole/V-dipole and the MAG boom are 74° and 68°, respectively, leading to a lesser coupling with the boom as discussed in Section 4.1.

We note that the effective length vectors above quasi-static frequencies are neither constant nor real-valued anymore, but they are complex-valued and also depend on the incoming direction of the wave. It is thus not possible anymore to do proper direction-finding above the so-called quasi-static frequency range. Therefore, we shortly investigate the properties of the transfer matrices from 500 kHz to 6 MHz in 500 kHz steps to find the upper frequency limit of the quasi-static frequency range.

The left panel of Figure 6 shows the changes of the colatitudes and azimuths of the effective lengths vectors with frequency. We have taken the values at 500 kHz as the basis, and the real part of the transfer matrix was taken for the calculation of these angles and their respective differences to the corresponding value at 500 kHz. One can see that there are significant changes above ~3 MHz (3,000 kHz). Only the colatitude of the U-dipole starts to show changes at even lower frequencies and is already beyond 2° at 2 MHz. Hence, to achieve an accuracy of direction-finding of ~2° it is advisable to restrict it to frequencies below 1,500 kHz. The right panel of Figure 6 shows the standard deviations of the angles of the effective length vectors as a function of frequency. Since the transfer matrices start to depend on the incoming direction of the radio

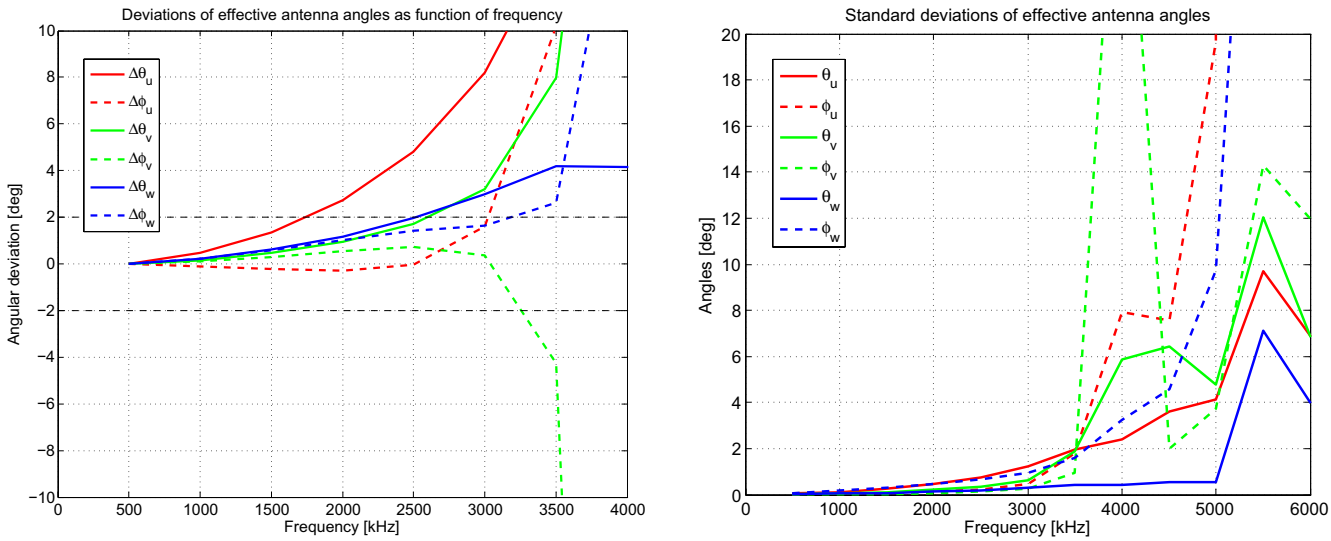


Figure 6. The left panel shows deviations of the mean colatitudes ($\Delta\theta$) and azimuths ($\Delta\phi$) of the effective length vectors for the U-dipole (in red), the V-dipole (in green), and the W-dipole (in blue) as a function of frequency from the corresponding values at 500 kHz. Deviations of $\pm$ 2° are marked by a dashed line. The right panel shows the standard deviation of the effective angles for 14 different incoming wave directions as a function of frequency.

wave with increasing frequencies, we have calculated them for 14 different directions. These were the 3 coordinate axes in both directions $[(\pm1,0,0),(0,\pm1,0),(0,0,\pm1)]$ plus the eight possible permutations of the space diagonal $(\pm1,\pm1,\pm1)$. The left panel of Figure 6 is based on the mean value of these 14 directions, whereas the standard deviations are shown in the right panel of the same figure. One can see here that for frequencies higher than 3.5 MHz these standard deviations have high values exceeding 2°, which means there is a significant directional dependence of the effective antennas above 3.5 MHz. In principle it would be possible to do direction-finding also from 1.5 to 3.5 MHz, but it would be needed use different effective length vectors for each frequency according to the left panel of Figure 6.

In Figure 7 we show the far-field total gain patterns for the U-dipole (left column), the V-dipole (middle column), and the W-dipole (right column) at frequencies of 1 MHz (first row), 3 MHz (second row), and 8 MHz (third row). This is followed by Figure 8, in which the gain patterns for the frequencies of 18 MHz, 30 MHz, and 45 MHz (in rows) are shown for all three dipoles (in columns) similar to the previous figure. At 1 MHz the antenna system is in the quasi-static frequency range, so the shape of the gain patterns looks strictly toroidal. This can be seen in the first row of Figure 7, and at the U-dipole we have also indicated the direction of the effective length vector, which is equivalent to the direction of the minimum gain. Some slight distortions from the toroidal shape can already be seen at a frequency of 3 MHz (second row of Figure 7), especially for the V-dipole in the middle panel. At 8 MHz (third row of Figure 7) the patterns already have multiple lobes except for the V-dipole, where they show up around 18 MHz (middle panel of first row in Figure 8). The number of lobes is progressively increasing at the higher frequencies of 30 and 45 MHz (second and third row of Figure 8). For the higher frequencies the patterns are strongly frequency dependent and have intricate shapes with several lobes, precluding accurate direction finding of the observed radio sources. Figures 7 and 8 show that above the quasistatic region the sensitivity of the dipoles is mostly higher for waves coming from the +x hemisphere. This gives evidence that the SP have a slight shielding effect against waves incident from the −x hemisphere.

For the quasi-static frequency range we have a high antenna gain towards the positive z direction for U and V-dipole, see first row of Figure 7. This is important because the optical instruments of JUICE are looking towards this direction, and so the spacecraft's attitude will often be such that Jupiter and its radio sources are located towards the $+z$ direction. The gain of the W-dipole in $+z$ direction is somewhat smaller, but its long effective length will still enable a good direction-finding together with the other two antennas. Furthermore, the almost perpendicular effective axes of the U and V-dipole should preferably be used for wave polarization measurements, which should work very well for a radio source in $+z$ direction. We finally note

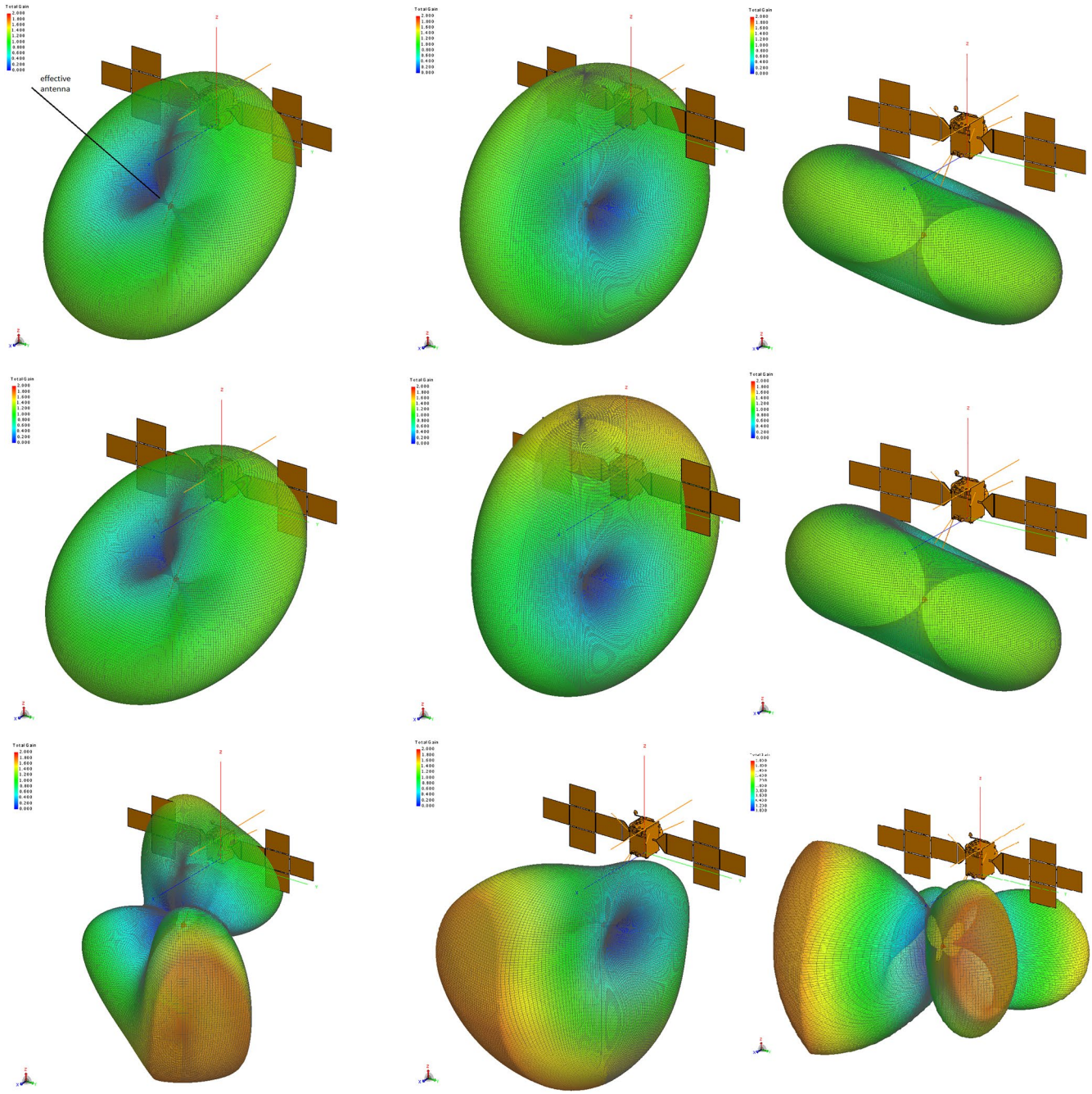


Figure 7. Far-field gain patterns for 1 MHz (first row), 3 MHz (second row), and 8 MHz (third row) for U-dipole (left panels), V-dipole (middle panels) and W-dipole (right panels). The color scales go from 0 (dark blue) to 2 (red) and denote the total linear gain.

again that reliable results for direction-finding with an accuracy of at least 2° can only be achieved below 1.5 MHz with the JUICE RWI antenna system.

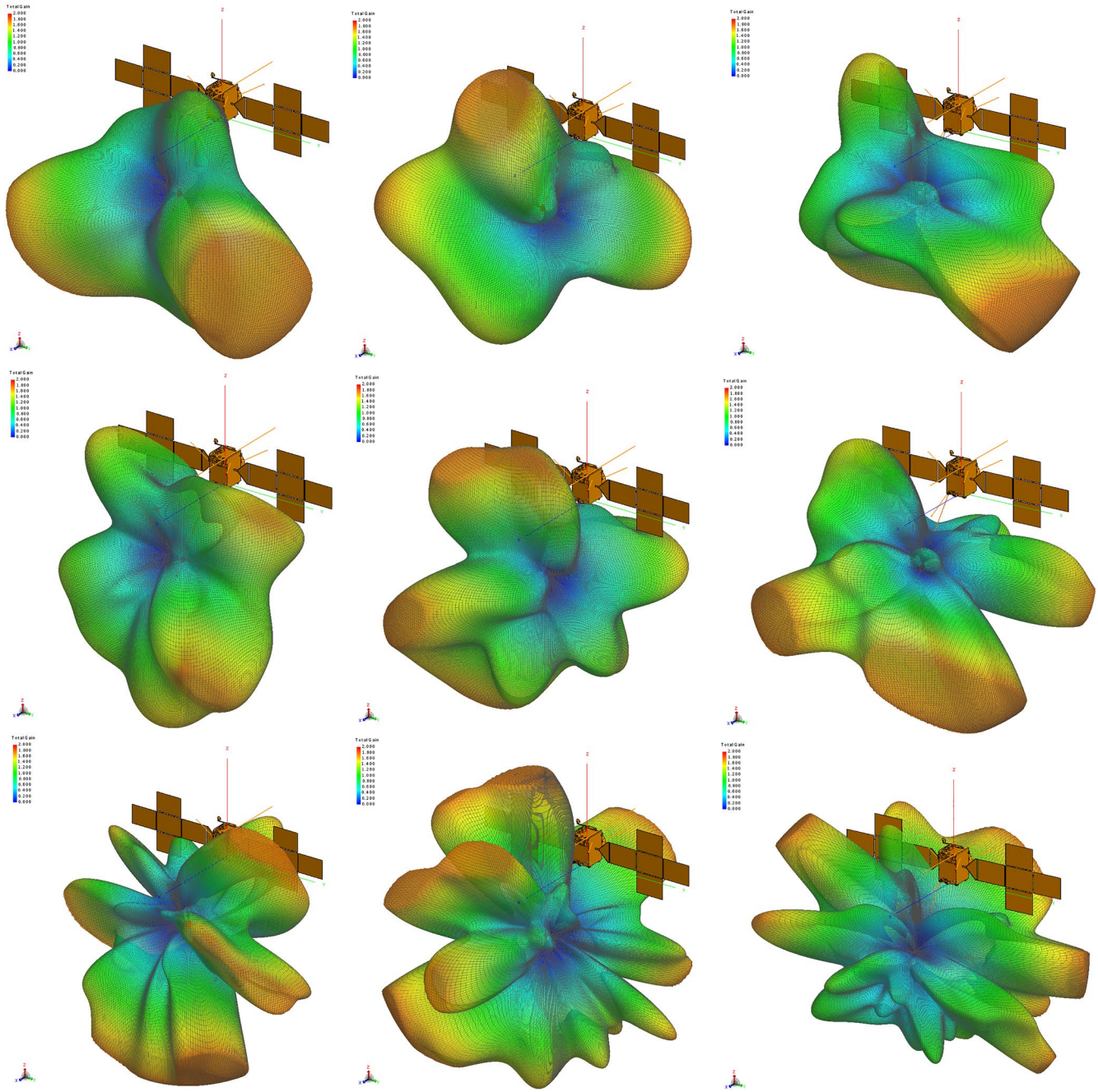


Figure 8. Far-field gain patterns for 18 MHz (first row), 30 MHz (second row), and 45 MHz (third row) for U-dipole (left panels), V-dipole (middle panels) and W-dipole (right panels). The color scales go from 0 (dark blue) to 2 (red) and denote the total linear gain.

6. Influence of Other Spacecraft Instruments on RPWI

6.1. The Influence of the Active Radar on the Passive RPWI Sensors

The RIME (Radar for Icy Moons Exploration) instrument is an ice-penetrating radar to study the subsurface structure of the Jovian icy moons down to a depth of about 9 km with a vertical resolution up to 30 m in ice. RIME works at a central frequency of 9 MHz with bandwidths of either 1 MHz or 3 MHz. Its emitted power will be 10 W (Dirk Plettemeier, personal communication). RIME uses a dipole with a tip-to-tip length of

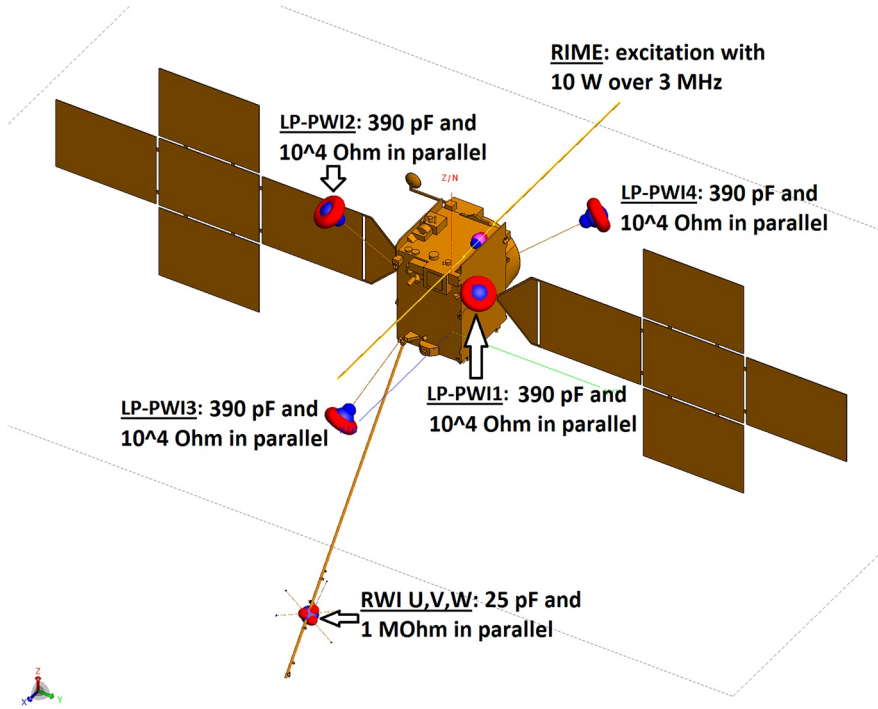


Figure 9. Jupiter Icy Moons Explorer spacecraft model for the calculation of the influence of the radar antenna Radar for Icy Moons Exploration (RIME) on the e Radio and Plasma Wave Investigation sensors. The RIME antenna (drawn in yellow) is excited with a radiated power of 10 W over a 3 MHz bandwidth. There are four Langmuir Probe ports (LP-PWI 1 to 4) and 3 RWI ports (U, V, W) with certain impedances at which voltages and currents are induced.

16 m, and it is mounted on the top platform of the spacecraft bus parallel to the *x*-axis of the main spacecraft coordinate system (see Figure 1 or 9).

In Figure 9 we can see a total number of eight ports. For our simulation only the port of the RIME antenna is active, and all the other ports are passive. The RIME antenna is driven by a voltage of a few tens of Volts that corresponds to a total radiated power of 10 W. The half-wavelength antenna resonance of the 16 m tip-to-tip dipole (32 m wavelength) should be at 9.375 MHz. We added a capacitive load of 0.73 nF in order to have the antenna resonance at the central frequency of 9 MHz which is characterized by a vanishing imaginary part of the impedance. The real part of the RIME antenna impedance at 9 MHz was found to be around 61 Ohms, close to the theoretical value of 73 Ohms of a stand-alone half-wave dipole. We excited the antenna with a radiated power of 10 W over a bandwidth of 3 MHz from 7.5 to 10.5 MHz. This corresponds to a spectral power of 3.3×10^{-6} W Hz^{-1}, or a power of 0.67 W over a bandwidth of 200 kHz. RWI has a frequency sweeping receiver with a bandwidth of ~200 kHz, and so a RIME radiated power of 0.67 W can induce a certain voltage in each RWI antenna over each 200 kHz bandwidth from 7.5 to 10.5 MHz. The strong RIME excitation causes a large electric near field and strong surface currents of up to 1 A m^{-1} close to the RIME ports, whereas typical surface currents are around 0.01 A m^{-1} on the MAG boom and around 1 mA m^{-1} on the RWI antennas. We calculated the induced voltages and currents at the four Langmuir Probe ports LP-PWI 1–4 (Langmuir Probe Plasma Wave Instrument) and for the three RWI ports, and those values crucially depend on the respective port impedance. For the Langmuir Probe ports an equivalent circuit diagram (Jesper Fredriksson, personal communication) shows that a load of 390 pF in parallel to 10 kΩ should be applied. For the RWI ports it is the base capacitance of 25 pF in parallel to a resistor of 1 MΩ, with the latter being a large dropping resistor in series with the pre-amplifier.

Figure 10 shows the induced voltages at the Langmuir Probe ports (LP-PWI) on the left side and the induced currents on the right side. It can be seen that the voltages are ~20 mV at most, and that the currents are not higher than ~0.5 mA. This means that for voltage and current in phase the deposited power should be ~5 μW at most. However, as voltage and current are close to quadrature, the FEKO calculation for the depos-

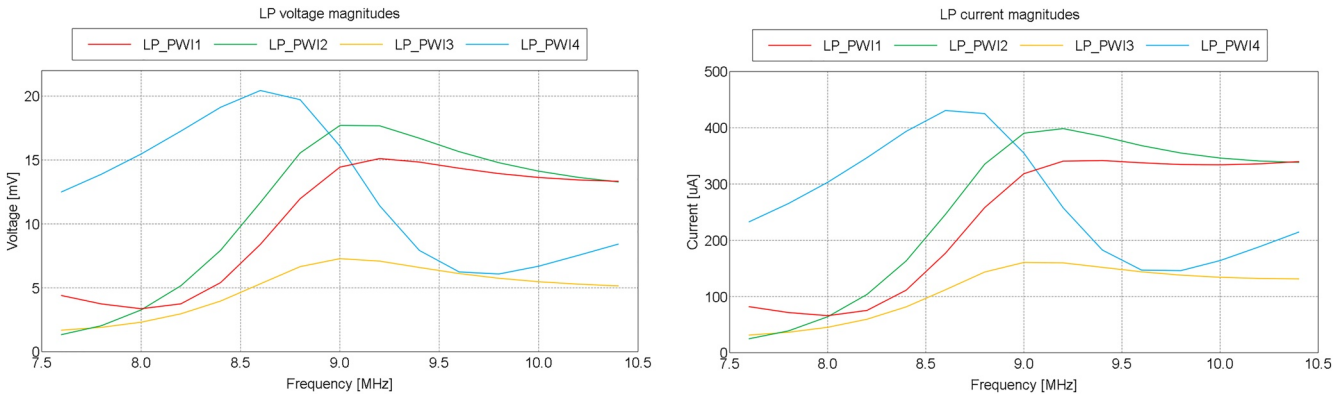


Figure 10. Voltages (left) and currents (right) induced in a 200 kHz band by a strong RIME radar antenna signal at all four Langmuir Probe ports (loaded with 390 pF and 10^4 Ohms in parallel) as a function of center frequency from 7.6 to 10.4 MHz.

ited power gives a maximum of only ~30 nW. The voltages and currents at LP-PWI 3 are about three times smaller than for the other probes. This is not surprising as LP-PWI 3 has the largest distance to the RIME antenna (see Figure 9), whereas the distances of LP-PWI 1, 2, and 4 to the RIME antenna are almost similar.

For the RWI antennas in Figure 11 the induced voltages are ~0.3 V at most, and the currents are always under ~0.5 mA. Due to the capacitive antenna voltage and currents are close to quadrature, and therefore the FEKO calculations yields a maximum for the deposited power of just ~50 nW. The largest voltages and currents occur for the W-antenna, which should have the same reason as discussed at the end of Section 4.1: The small angular separation between the W-antenna and the MAG boom (compared to U and V-dipole) should lead to larger induced voltages and currents for the W-antenna.

These calculations have shown us that the induced voltages and currents should be no harm for the instruments, neither for the Langmuir Probes, nor for the RWI antennas. Some elements in the RWI and LP pre-amplifiers (diodes) are only able to withstand a power input of ~100 mW, and our calculation has shown that the deposited power is only of the order of tens of nW. Even if the power of 10 W is emitted over a bandwidth of just 1 MHz (and not 3 MHz), the deposited power should just be a factor of three larger. We also note that the transceiver for the Langmuir Probes just goes up to a frequency of 1.5 MHz, and at this frequency the power output of RIME should be several tens of dB smaller due to the filters of the RIME impedance matching network.

The large RIME signal will of course be detectable by the RWI antennas and saturate its receiver when transmitting. The sensitivity of the RWI antennas is around 10 nV m^{-1} $Hz^{-1/2}$. Using a bandwidth of 200 kHz and an effective length of ~1 m, we find that the smallest detectable voltage signal is ~5 μ V. This means

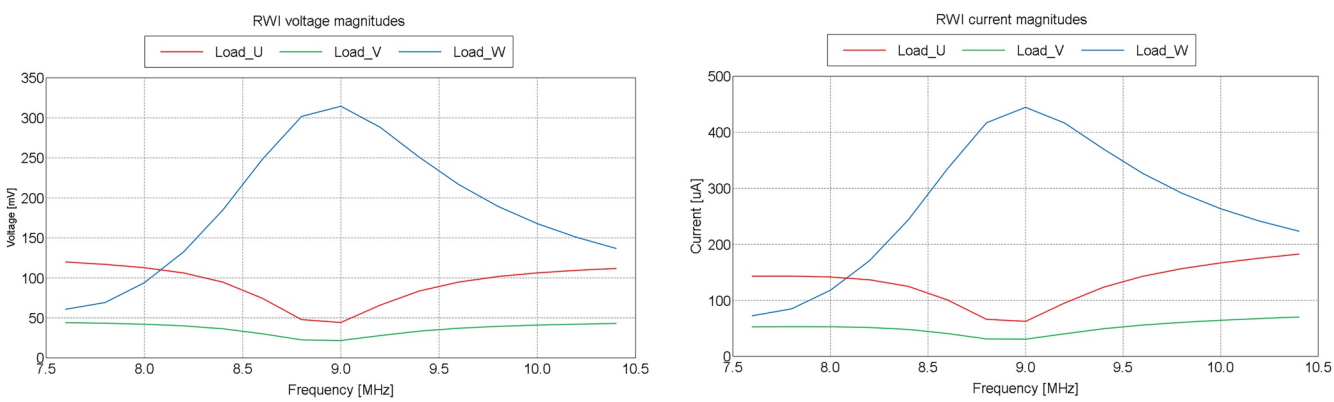


Figure 11. Voltages (left) and currents (right) induced in a 200 kHz band by a strong Radar for Icy Moons Exploration radar antenna signal at all three Radio Wave Instrument antenna ports (loaded with 25 pF and 10^6 Ohms in parallel) as a function of center frequency from 7.6 to 10.4 MHz.

Table 4
Spherical Coordinates of Physical Antennas in Comparison to Open and Loaded Port Effective Length Vectors for U, V, and W Dipole

	Physical antennas			Open ports				Loaded ports (25 pF)			
Antenna name	h [m]	θ [deg]	ϕ [deg]	h^o [m]	θ^o[deg]	ϕ^o [deg]	γ^o[deg]	h^l [m]	θ[deg]	ϕ^l [deg]	γ^l[deg]
U + U−	2.5	69.6	−22.1	1.07	44.6	−25.7	25.1	0.26	45.1	−25.9	24.7
V + V−	2.5	98.1	64.9	0.92	85.4	72.5	14.8	0.23	84.8	73.1	15.6
W + W−	2.5	22.1	134.4	1.87	27.6	156.3	10.6	0.48	27.7	155.9	10.6

Note. For the loaded port a base capacitances of 25 pF was used. The letter h denotes the effective length, the angle θ is the colatitude, and ϕ is the azimuth. The superscripts "o" and "l" denote the values for open ports and loaded ports, respectively. The angle γ gives the angular deviations of the effective antennas from the physical ones.

that the voltage pulse from RIME should be about a factor of ~10^5 higher than the RWI sensitivity. The RWI has no automatic gain control, and the 14-bit ADC (Analog-to-Digital Converter) has a dynamic range of $2^{14} = 16,384$. Therefore, the RIME signal should still be a factor of ~6 above the RWI saturation level. As a consequence, no scientific observations are possible for the RWI during active RIME periods. However, RIME will mostly be used for only brief periods of time around the closest approaches to icy satellites. Many RIME observations will be done at the far side of the moons seen from Jupiter during which the strong Jovian radio emissions are obscured and cannot be detected by the RWI instrument anyway. Additionally, for some passes at the near side during which the Jovian radio emissions can be detected, it is planned to use them as a natural tool for radio sounding. Then RIME will be in a passive mode and no active signals disturbing the RWI observations will be emitted (Kumamoto et al., 2017; Romero-Wolf et al., 2015; Schroeder et al., 2016). As the RWI will be turned on during most of the time and the closest approach times to moons are not special for the observation of Jovian radio emissions, the scientific impact of not being able to make RWI observations during active RIME periods should be very small.

6.2. The Influence of the JENI Instrument on the RPWI Sensors

The JENI (Jovian Energetic Neutrals and Ions) instrument on-board JUICE has a high voltage power source that provides a voltage of 8 kV to a set of plates. The voltage source has a ripple (AC fluctuation) of about 1.3 V at a frequency of 100 kHz (Pontus Brandt, personal communication). However, the fluctuation should be decreased by an output filter by at least a factor of 100, so the ripple should typically be ~13 mV. We modeled the spacecraft in the same way as in the previous subsection with the same RWI and Langmuir probe impedances as given in Figure 9. Only the JENI instrument was modeled in more detail, and it was designed without the protective grid covering its plates. We applied a voltage with an amplitude of 13 mV at the JENI plates with a frequency of 100 kHz. We found that the induced surface currents by the AC fluctuation are just as high as 10^{-9} A m^{-1} close to the JENI plates. Further away, the induced surface currents on the RWI antennas and the LP are much smaller and around 10^{-20} A m^{-1}. The induced voltages and currents at the RWI and Langmuir Probe ports are only of the order of 0.1 μV and 1 pA, respectively. This small voltage and current is absolutely no harm to the RPWI sensors, and it won't even cause a measurable signal. The smallest detectable voltage signal for RWI is ~5 μV, which is more than one order of magnitude larger than the induced signal. So even when the JENI output filter fails, the signal from the ripple will barely be detectable. This is similar for the Langmuir Probes as their sensitivity is even smaller than the one of the RWI antennas.

7. Discussion and Conclusions

Table 4 summarizes the results of our effective length vector calculations. We give the spherical coordinates of the physical antennas, and of the open and loaded port effective antennas for JUICE RWI. The latter have been calculated for a quasi-static frequency of 300 kHz, and we also indicate the angles γ between the physical and effective antennas for all three dipoles.

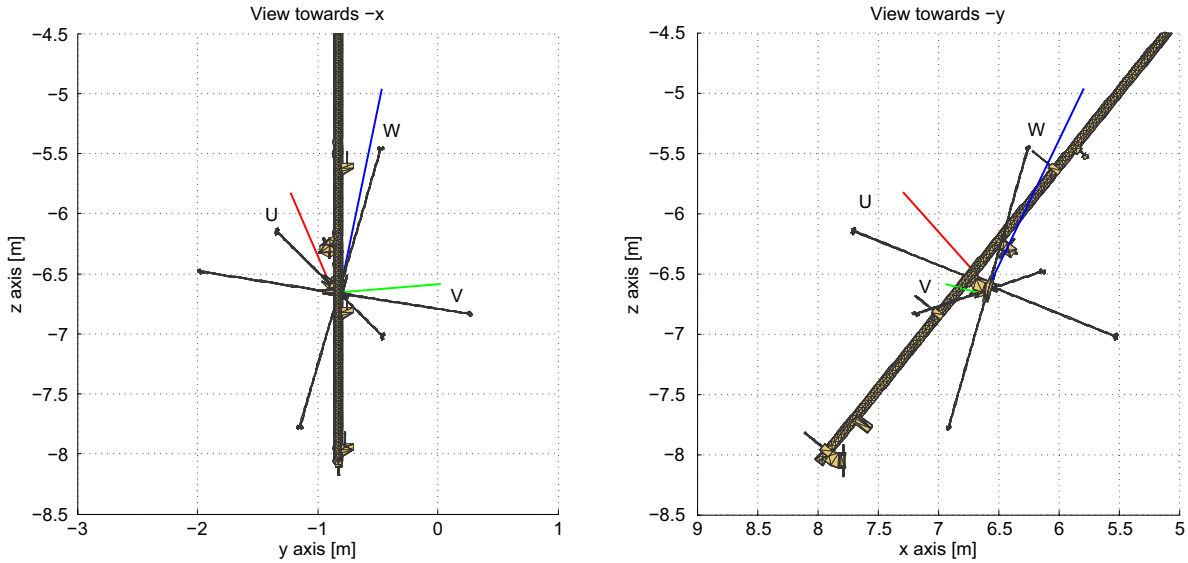


Figure 12. Drawing of physical and effective antennas for open ports at a quasi-static frequency of 300 kHz. The effective antennas are in red for the U-dipole, in green for the V-dipole, and in blue for the W-dipole, and they are drawn at the U+, V+, W+ side of the respective antenna. The view on the left goes along the *x*-axis towards negative values, and the view on the right goes along the *y*-axis towards negative values.

The three physical antennas are perpendicular to each other. The open port effective length vectors have the following angular separations between each other: The angle between U and V-dipole is 92.5°, the angle between U and W-dipole is 72.2°, and the one between V and W-dipole is 83.1°. For the 25 pF loaded ports these angular deviations change to 92.6° (U–V), 72.7° (U–W), and 82.1° (V–W), respectively. Hence, the three dipoles should have a sufficient angular separation for proper a direction-finding of incoming radio waves. The angular deviations between the physical and effective antennas given by the angle γ in Table 4 range from 10° to 25°. A drawing showing these deviations is given in Figure 12. It is obvious from this figure as well as from Table 4 that the effective length of the W-dipole is almost twice as long as of U or V-dipole. The reason for this is most likely that the currents on the MAG boom induce larger currents in the W-dipole, since the angle between W-dipole and MAG boom is just ∼28°, whereas the angles between the U-dipole/V-dipole and the MAG boom are ∼74° and ∼68°, respectively. The inclusion of loaded ports changes the effective antenna directions by a few tenth of a degree, and the maximum deviation can be seen in Table 4 for the colatitude and azimuth of the V-dipole which both change by 0.6°. However, the effective lengths are changing considerably when a capacitive load is added to the antenna as the ratio of open to loaded port effective length is approximately given by $C_A/(C_A + C_L) = 8/(8 + 25) = 0.24$.

We note that initially the SP were planned to be larger, consisting of 10 panels of 2.5 m × 4.0 m (and not just 2.5 m × 3.5 m as now) giving a total area of 100 m^2. This meant a spacecraft that would have been ∼3 m longer along the *y* direction, or ∼1.5 m on each side. Our initial calculations did use such large SP, and the angles of the effective antennas were up to 4° different compared to the results for the smaller panels presented in this paper. This means that the two main elements of the spacecraft with a large influence on the antenna reception properties are the nearby long magnetometer boom and the large SP. The modeling of the MAG boom is also crucial, since it is the closest element to the RWI antennas. We also calculated models in which the mesh of the cylindrical MAG boom only had a pentagonal cross-section. Our main model had a finer mesh for the MAG boom with an octagonal cross-section, and the difference in effective antenna angles compared to the pentagonal cross-section was up to 3°. Other modifications of the mesh, like a coarser grid for the SP or the central spacecraft body with a few thousand triangles less, only resulted in differences of a few tenth of a degree for the effective antenna angles. Finally, only the comparison with a future in-flight calibration of the RWI antennas will allow us to judge the absolute error of our modeling. We estimate that the angular error for the effective antenna directions presented in this paper should be around 1° to 2°. This estimation comes from the comparison of in-flight calibration results with numerical modeling for other spacecraft like Cassini (Vogl et al., 2004) or STEREO (Panchenko et al., 2014).

In Section 4.2 we have calculated the influence of the JUICE solar panel rotation on the effective antenna directions and length. The length changes only minimal (just 1 cm at most), but the angles can change by almost 1°. If the assumed angular error is around 1° to 2° as just mentioned above, does it make sense to look at such smaller changes? We think yes, because of the following reasons: First of all, it is of interest to get a rough idea how much the effective angles change with solar panel rotation. And second, it should be possible to largely eliminate systematic model errors by subtracting the results of two slightly different simulations at two different solar panel rotation angles from each other. This is exactly what we do in Figure 4 when relating all the changes in effective angles to the default position at 0° rotation angle. Finally, the in-flight calibration can tell us the correct effective length vectors of the antennas for the real spacecraft at the default position of the SP, and then Figure 4 can be used for small corrections if the SP are at different positions. Our simulations thus also tell us that it would be useful to perform the in-flight calibration at a constant solar panel position. During the calibration roll maneuvers it would be practical to use the default position in which the panels look into the same direction as the HGA as shown in Figure 1. Otherwise, the errors of the in-flight calibration could increase by up to 1°. Our numerical simulations are probably the only way to find the influence of the solar panel rotation on the effective antenna directions. This is due to the fact that it would be impracticable to perform separate calibrations for many different solar panel positions.

The most important result of our effective length vector calculations at higher frequencies in Section 5 is that it is not recommended to do radio wave direction-finding above a frequency of ~1.5 MHz. This is similar to the Cassini RPWS antennas, despite the fact that the Cassini monopoles are four times longer than the RWI dipole tip-to-tip length. We had hoped that direction-finding for JUICE RWI would also be possible at somewhat higher frequencies, as the antenna resonance is at much higher frequencies (60 MHz) and as dipoles are usually less influenced by the spacecraft structure than monopoles. However, the simulations give evidence that mainly the size of the whole spacecraft (and not just the antennas) in relation to the wavelength determines at which frequencies the effective length vectors are not constant anymore. Our antenna gain plots in Figures 7 and 8 have shown that some distortions from the toroidal gain shape of the dipole already occur at 3 MHz, and that multiple lobes first show up around 8 MHz. Not only the gain, but also the wave polarization sensitivity of the antennas are extremely direction-dependent for frequencies above 5 MHz.

We also used numerical simulations to estimate the influence of other instruments on antennas as well as LP sensors and receivers. We found that voltage ripples in the high-voltage JUICE JENI instrument should have no influence, but the strong 10 W active radar pulses of RIME around 9 MHz will saturate the RWI receiver. However, the deposited power from the strong RIME signal is just of the order of tens of nW for LP and RWI antennas. This should do no harm. It is planned to perform a RIME interference measurement campaign, to further evaluate the influence of active RIME transmission on other instruments and measurements.

Data Availability Statement

No measurement data was needed for this publication. The detailed CAD model of the JUICE spacecraft is proprietary to Airbus. However, the main and relevant geometrical features of our reduced model are well described in Section 3.

Acknowledgments
G. Fischer and M. Panchenko acknowledge support from the Austrian Space Applications Program (ASAP 13) of the Austrian Research Promotion Agency (FFG) under project 859728 named "Experimental and numerical models for the calibration of the JUICE RWI antennas." They also acknowledge support from ESA Prodex for the project JUICE-RWI-ORIENT (no. 4000118632), which was performed to find the optimum orientation of the JUICE RWI antenna triad on the magnetometer boom (see Section 3.3 of this paper). The development of RWI at Astronika was financed by ESA Prodex under project no. 4000119065/16/NL/JK. Astronika's engineers who greatly contributed to development of the RWI antennas are: Jerzy Grygorczuk, Piotr Palma, Stanisław Jarzynka, Tomasz Kuciński, Maciej Ossowski, Mateusz Duda, Karol Jarocki, Henryk Gut, Michał Bogoński, Dominik Nolbert, Ewelina Ryszawa, Paweł Miara, Kamil Bochra, Mateusz Grzyb, Przemysław Nowotarski, Maciej Ataman, and Sławomir Szczyglak. The Swedish National Space Agency (SNSA) is the lead agency for, and supports, the JUICE/RPWI instrument implementation. The Swedish Institute of Space Physics (IRF) in Uppsala supports and manages the JUICE/RPWI instrument implementation as the Principal Investigator (PI) institute. The JAXA, the Polish PRODEX committee, and CNES also supported the RWI subsystem implementation.

References

Carozzi, T., Karlsson, R., & Bergman, J. (2000). Parameters characterizing electromagnetic wave polarization. *Physical Review E-Statistical Physics, Plasmas, Fluids, and Related Interdisciplinary Topics*, *61*(2), 2024–2028. https://doi.org/10.1103/PhysRevE.61.2024

Cecconi, B., & Zarka, P. (2005). Direction finding and antenna calibration through analytical inversion of radio measurements performed using a system of two or three electric dipole antennas on a three-axis stabilized spacecraft. *Radio Science*, *40*(3), RS3003. https://doi.org/10.1029/2004RS003070

Fischer, G., Cecconi, B., Bergman, J., Girard, J., Quinsac, G., & Wahlund, J. E. (2017). Short antennas on a large spacecraft. In G. Fischer, G. Mann, M. Panchenko, & P. Zarka (Eds.), *Planetary radio emissions VIII* (pp. 515–523). https://doi.org/10.1553/PRE8s515

Fischer, G., Macher, W., Rucker, H. O., Ladreiter, H. P., & Vogl, D. F., & Cassini/RPWS Team. (2001). Wire-grid Modeling of Cassini Spacecraft for the determination of effective antenna length vectors of the RPWS antennas. In *Planetary radio emissions V* (pp. 347–356).

Grasset, O., Dougherty, M. K., Coustenis, A., Bunce, E. J., Erd, C., Titov, D., et al. (2013). JUpiter ICy moons Explorer (JUICE): An ESA mission to orbit Ganymede and to characterise the Jupiter system. *Planetary and Space Science*, *78*, 1–21. https://doi.org/10.1016/j.pss.2012.12.002

Gurnett, D. A., Scarf, F. L., Kurth, W. S., Shaw, R. R., & Poynter, R. L. (1981). Determination of Jupiter's electron density profile from plasma wave observations. *Journal of Geophysical Research*, *86*(A10), 8199–8212. https://doi.org/10.1029/JA086iA10p08199

Harrington, R. F. (1968). *Field computation by moment methods*. Robert E. Krieger Publishing Company.

Jackson, J. D. (1975). *Classical electrodynamics*. J. Wiley and Sons.

Kraus, J. D. (1966). *Radio astronomy*. McGraw-Hill.

Kumamoto, A., Kasaba, Y., Tsuchiya, F., Misawa, H., Kita, H., Puccio, W., & Kobayashi, T. (2017). Feasibility of the exploration of the subsurface structures of Jupiter's icy moons by interference of Jovian hectometric and decametric radiation. In G. Fischer, G. Mann, M. Panchenko, & P. Zarka (Eds.), *Planetary radio emissions VIII* (pp. 127–136). https://doi.org/10.1553/PRE8s127

Ladreiter, H. P., Zarka, P., Lecacheux, A., Macher, W., Rucker, H. O., Manning, R., et al. (1995). Analysis of electromagnetic wave direction finding performed by spaceborne antennas using singular-value decomposition techniques. *Radio Science*, *30*(6), 1699–1712. https://doi.org/10.1029/95RS02479

Macher, W. (2008). *Transfer matrix description of multi-port antennas and its application to the Mars Express/MARSIS radar* (Unpublished doctoral dissertation). PhD thesis, Graz Technical University.

Macher, W. (2012). Interreciprocity principles for linear network-waveguides systems based on generalized scattering, admittance and impedance matrices. *IEEE Transactions on Circuits and Systems*, *59*(4), 721–734. https://doi.org/10.1109/tcsi.2011.2169888

Macher, W., Oswald, T. H., Fischer, G., & Rucker, H. O. (2007). Rheometry of multi-port spaceborne antennas including mutual antenna capacitances and application to STEREO/WAVES. *Measurement Science and Technology*, *18*(12), 3731–3742. https://doi.org/10.1088/0957-0233/18/12/008

Macher, W., Plettemeier, D., Rucker, H. O., & Fischer, G. (2006). Wire-Grid Simulations of the Mars Express/MARSIS Antenna System. In *Planetary radio emissions VI* (pp. 483–490).

Oswald, T. H., Macher, W., Fischer, G., Rucker, H. O., Bougeret, J. L., Kaiser, M. L., & Goetz, K. (2006). Numerical analysis of the STEREO WAVES Antennas: First results. In *Planetary radio emissions VI* (pp. 475–482).

Oswald, T. H., Macher, W., Rucker, H. O., Fischer, G., Taubenschuss, U., Bougeret, J. L., et al. (2009). Various methods of calibration of the STEREO/WAVES antennas. *Advances in Space Research*, *43*(3), 355–364. https://doi.org/10.1016/j.asr.2008.07.017

Panchenko, M. (2004). Polarimetry of auroral kilometric radiation with a triaxial nonorthogonal antenna system. *Radio Science*, *39*(6), RS6010. https://doi.org/10.1029/2004RS003039

Panchenko, M., Macher, W., Rucker, H. O., Fischer, G., Oswald, T. H., Cecconi, B., & Maksimovic, M. (2014). In-flight calibration of STEREO-B/WAVES antenna system. *Radio Science*, *49*(3), 146–156. https://doi.org/10.1002/2013RS005197

Rief, G. (2013). *Numerical calibration of the Cassini RPWS antenna system* (Unpublished doctoral dissertation). MSc thesis, Karl-Franzens-University of Graz.

Romero-Wolf, A., Vance, S., Maiwald, F., Heggy, E., Ries, P., & Liewer, K. (2015). A passive probe for subsurface oceans and liquid water in Jupiter's icy moons. *Icarus*, *248*, 463–477. https://doi.org/10.1016/j.icarus.2014.10.043

Rucker, H. O., Macher, W., Fischer, G., Oswald, T., Bougeret, J. L., Kaiser, M. L., & Goetz, K. (2005). Analysis of spacecraft antenna systems: Implications for STEREO/WAVES. *Advances in Space Research*, *36*(8), 1530–1533. https://doi.org/10.1016/j.asr.2005.07.060

Rucker, H. O., Macher, W., Manning, R., & Ladreiter, H. P. (1996). Cassini model rheometry. *Radio Science*, *31*(6), 1299–1311. https://doi.org/10.1029/96RS01972

Sampl, M., Macher, W., Gruber, C., Oswald, T., Kapper, M., Rucker, H. O., & Mogilevsky, M. (2015). High-frequency performance of electric field sensors aboard the RESONANCE satellite. *Geoscientific Instrumentation, Methods and Data Systems*, *4*(1), 81–88. https://doi.org/10.5194/gi-4-81-2015

Sampl, M., Macher, W., Gruber, C., Oswald, T., Rucker, H. O., & Mogilevsky, M. (2012). Calibration of electric field sensors onboard the resonance satellite. *IEEE Transactions on Antennas and Propagation*, *60*(1), 267–273. https://doi.org/10.1109/TAP.2011.2167918

Sampl, M., Macher, W., Oswald, T., Plettemeier, D., Rucker, H. O., & Kurth, W. S. (2016). Juno model rheometry and simulation. *Radio Science*, *51*(10), 1627–1635. https://doi.org/10.1002/2016RS005954

Sampl, M., Rucker, H. O., Oswald, T. H., Plettemeier, D., Maksimovic, M., & Macher, W. (2011). Numerical simulations of the Solar Orbiter antenna system RPW ANT. In H. O. Rucker, W. S. Kurth, P. Louarn, & G. Fischer (Eds.), *Planetary radio emissions (pre VII)* (pp. 487–494). https://doi.org/10.1553/pre7s487

Schroeder, D. M., Romero-Wolf, A., Carrer, L., Grima, C., Campbell, B. A., Kofman, W., et al. (2016). Assessing the potential for passive radio sounding of Europa and Ganymede with RIME and REASON. *Planetary and Space Science*, *134*, 52–60. https://doi.org/10.1016/j.pss.2016.10.007

Sinclair, G. (1950). The transmission and reception of elliptically polarized waves. *Proceedings of the IRE*, *38*, 148–151. https://doi.org/10.1109/jrproc.1950.230106

Vogl, D. F., Cecconi, B., Macher, W., Zarka, P., Ladreiter, H. P., Fédou, P., & Hospodarsky, G. B. (2004). In-flight calibration of the Cassini-Radio and Plasma Wave Science (RPWS) antenna system for direction-finding and polarization measurements. *Journal of Geophysical Research*, *109*(A9), A09S17. https://doi.org/10.1029/2003JA010261